

Variability of urban surface temperatures and implications for aerodynamic energy exchange in unstable conditions

Article

Accepted Version

Crawford, B., Grimmond, S. B. ORCID: <https://orcid.org/0000-0002-3166-9415>, Gabey, A., Marconcini, M., Ward, H. C. and Kent, C. W. (2018) Variability of urban surface temperatures and implications for aerodynamic energy exchange in unstable conditions. Quarterly Journal of the Royal Meteorological Society, 144 (715). pp. 1719-1741. ISSN 1477-870X doi: 10.1002/qj.3325 Available at <https://centaur.reading.ac.uk/77578/>

It is advisable to refer to the publisher's version if you intend to cite from the work. See [Guidance on citing](#).

To link to this article DOI: <http://dx.doi.org/10.1002/qj.3325>

Publisher: Royal Meteorological Society

All outputs in CentAUR are protected by Intellectual Property Rights law, including copyright law. Copyright and IPR is retained by the creators or other copyright holders. Terms and conditions for use of this material are defined in the [End User Agreement](#).

www.reading.ac.uk/centaur

CentAUR

Central Archive at the University of Reading

Reading's research outputs online

Variability of urban surface temperatures and implications for aerodynamic energy exchange in unstable conditions

B. Crawford^{*1,2}, C.S.B. Grimmond¹, A. Gabey^{1,3}, M. Marconcini⁴, H.C. Ward^{1,5}, C. W. Kent¹

*Corresponding author

¹Department of Meteorology, University of Reading, UK

²Current affiliation: Department of Civil and Environmental Engineering, Massachusetts Institute of Technology, USA

³Current affiliation: Institute for Environmental Analytics, Reading, UK

⁴Remote Sensing Data Center, German Aerospace Center (DLR), Germany

⁵Current affiliation: Department of Atmospheric and Cryospheric Sciences, University of Innsbruck, Austria

Abstract

Sensible heat flux (Q_H) is a critical driver of surface and boundary layer meteorological processes, especially in urban areas. Aerodynamic resistance methods (ARM) to model Q_H are promising because, in principle, all that is needed is surface temperature (T_o), air temperature (T_A) and an aerodynamic resistance term (r_H). There are significant challenges in urban areas however, due to uncertainties in satellite-derived land surface temperatures (LST), logistical challenges to obtain high-resolution air temperatures, and limited understanding of spatial and temporal variability of r_H and associated variables (e.g. thermal roughness length). This work uses an extensive LST dataset covering six years (2011-2016) in central London and a long-term *in situ* observation network to analyse variability of LST and r_H variables. Results show that LST is spatially correlated with building and vegetation land cover with coherent thermal structures at length scales less than 500-1000 m. Additionally, satellite-observed LST varies with average building height (up to 10% cooler in areas with tall buildings). The r_H term and associated variables are observed to vary on daily and seasonal cycles and findings are used to model Q_H using five variations of an ARM-based approach on a 100 m pixel basis. Modelled Q_H is compared to observations from three scintillometer paths and an eddy covariance flux tower. We find generally good agreement between observations and models, though there is uncertainty in all methods (mean absolute error ranges from 58.1-129.3 $W m^{-2}$) due to challenges in determining high-resolution meteorological and surface inputs, particularly LST and friction velocity (u_*). Additional complexity in evaluating modelled Q_H arises from anthropogenic heat sources: long-term tower-based observations show that T_A and radiometer-derived T_o are warmer during working weekdays than non-working days (up to 0.7°C) and that there is an observed lag (2-3 hours) between energy consumption and observed warming and Q_H .

Keywords: urban meteorology, surface energy balance, remote sensing, observations

1. Introduction

Turbulent sensible heat flux (Q_H , $W m^{-2}$) is a dominant component of surface-atmosphere energy exchange in many cities due to relative lack of moisture and vegetation compared to non-urban environments. Knowledge of Q_H is important for modelling dynamic processes in the urban atmosphere and partitioning net energy exchange between additional surface energy balance processes. Q_H is also a fundamental driver of urban boundary layer growth and hence a primary control on variations in urban air quality.

Recent progress in modelling urban surfaces has highlighted uncertainties in determining Q_H using both multi-layer canopy and bulk models (Grimmond et al. 2011). Additionally, characterization of sub-kilometre variability of urban physical characteristics and its impact on energy fluxes is an ongoing challenge to parameterise urban turbulent flux terms for meso-scale models (Barlow et al., 2017). Alternative techniques that can calculate high-resolution (<1 km) Q_H are needed to compare with urban land surface models.

An aerodynamic resistance method (ARM) is a common approach for modelling surface fluxes and this technique continues to be used in current meso-scale numerical weather prediction models (Mahrt 1996, Chen et al. 2010). However, high-resolution (e.g. sub-city scale) application of this technique has been limited in cities due to the extreme heterogeneity of the urban surface at numerous length scales.

The bulk aerodynamic resistance approach is based on surface layer similarity theory where Q_H is calculated as:

$$Q_H = c_p \rho \frac{T_o - T_A}{r_H} \quad (1)$$

where c_p is heat capacity of air ($J kg^{-1} K^{-1}$), ρ is air density ($kg m^{-3}$), T_o is the aerodynamic surface temperature (K), T_A is air temperature (K), and r_H is the bulk aerodynamic resistance for heat ($s m^{-1}$) of the complete 3D urban surface.

The aerodynamic surface temperature (T_o) is the air temperature extrapolated logarithmically to the height level $z_d + z_H$, where z_d is displacement height and z_H is the roughness length for heat (e.g. Kanda et al. 2007). Practically, T_o is difficult to measure and is often replaced in eq. 1 with some other surface temperature, such as satellite-observed land surface temperature (LST), the radiative surface temperature (T_R) calculated from measurements of upwelling longwave radiation, or area-weighted facet-based complete surface temperatures from some combination of thermal camera measurements (Voogt and Grimmond 2000) and 3D surface models (Morrison et al. 2018).

Large diurnal variations in z_H have been observed previously in urban areas (Voogt and Grimmond 2000, Moriwaki and Kanda 2006, Kanda et al. 2007), as well as in bare soil and vegetated environments (Verhoef et al. 1997). Brutsaert and Sugita (1996) attribute this variation to changes in solar angle which leads to vertical movement of the heat source in the canopy through the day. A relation between z_H and solar angle was observed in a light industrial area of Vancouver, Canada (Voogt and Grimmond 2000), but not over a 1:5 scale urban model for a full year (Kanda et al. 2007). Other explanations for z_H variation include use of inappropriate surface temperatures (Kanda et al. 2007) or anisotropic effects of canopy vegetation (e.g. Qualls and Hopson 1998). Overall, these large diurnal variations are difficult to interpret and there is significant uncertainty in z_H derived from observations due to accumulated measurement and source area uncertainties. In a traditional Monin-Obukhov similarity theory (MOST) framework, the aerodynamic resistance term r_H (eq. 1) can be defined as (Verma, 1989):

$$r_H = \frac{1}{ku^*} \left[\ln \left(\frac{z'}{z_0} \right) - \Psi_h \left(\frac{z'}{L} \right) \right] + \frac{1}{ku^*} \ln \left(\frac{z_0}{z_H} \right) \quad (2)$$

where z_0 is the roughness length for momentum, $z' = z_m - z_d$ (z_m is measurement height), Ψ_h is a similarity theory stability function, L is the Obukhov Length, k is von Karman's constant (0.4), and u^* is friction velocity. For convenience, the ratio between z_0 and z_H is often defined as (Owen and Thomson 1963):

$$kB^{-1} = \ln \left(\frac{z_0}{z_H} \right) \quad (3)$$

Determining bulk values of r_H is challenging in urban areas due to the complex geometry and heterogeneous thermal properties of urban materials. Several studies have used observed Q_H , T_A , and T_R to solve for r_H using eq. 1. (e.g. Voogt and Grimmond 2000, Kanda et al. 2007, Lee et al. 2016). There are several sources of uncertainty using this approach: i) observed Q_H obtained from eddy covariance (EC) observations is thought to be typically underestimated by EC given the lack of energy balance closure (Wilson et al. 2001), ii) observations from EC sensors and radiometers are representative of different source areas (Schmid et al. 1991, Schmid 1994), and iii) errors are introduced to T_R calculations from choice of bulk emissivity values and radiometer bias towards vertically-facing roof and street surfaces (Voogt and Grimmond 2000). Furthermore, the r_H value is expected to vary in space and time through variability in u^* , z_0 , and z_H . Brutsaert (1982) used a theoretical relation to relate kB^{-1} (eq. 3) to the roughness Reynold's number (Re^*) for rough natural surfaces:

$$kB^{-1} = \alpha Re^{*0.25} - 2.0 \quad (4)$$

where:

$$Re^* = z_0 u^* / \nu \quad (5)$$

where ν is kinematic viscosity ($1.46 \times 10^{-5} \text{ m}^2 \text{ s}^{-1}$) and α is an empirical constant. Kanda *et al.* (2007) experimentally determined an urban value for α (1.6) using observations over a scale model of bluff body cubes. To our knowledge, only a few studies have used LST and an aerodynamic resistance approach to derive Q_H in cities (Kato and Yamaguchi 2005, Weng *et al.* 2014). These studies have produced realistic flux values; however, they are based on relatively few images and lack a measurement network with which to compare results. Overall, there remain challenges with using ARM in urban areas for several reasons: i) uncertainties from satellite-derived measurements from satellite view bias and variable surface bulk emissivity in cities, ii) challenges to resolve spatial variations in air temperature and other meteorological and surface variables needed to calculate resistance in eq. 2, and iii) incomplete theoretical understanding of how r_H , kB^{-1} , and z_H vary in space and time under different flow and surface forcing conditions.

In this work, we attempt to calculate high-resolution Q_H based on a large dataset of EO-derived LST measurements and assess uncertainties with using an aerodynamic resistance approach. First, we analyse spatial LST patterns and characterize temporal variability of relevant variables, including r_H , kB^{-1} , and z_H , based on *in situ* observations at an eddy covariance tower. Next, five different variations to calculate r_H based on observations and statistical relations from the literature are tested and compared. Model uncertainty is evaluated using a Monte Carlo sampling approach of input variables. Central London is used as the test area for developing our methodology because of the presence of a long-term observation network of scintillometers and EC to enable direct comparison of observed and modelled Q_H .

2. Methods

2.1 Study domain

The focus of this study is London, UK; the most populous city in Europe (~8.9 million in Greater London Area [GLA, 2017]) and one of three study sites for the H2020 UrbanFluxes project (Chrysoulakis et al. 2015). The spatial domain is a 21.5 km x 21.4 km area encompassing central London (273591.1-295091.1 m E, 5701474-5722874 m N, UTM zone 31, WGS84, Figure 1). All analysis is performed on a 100 m x 100 m pixel basis to conform to Landsat-8 TIRS sensor resolution (Section 2.3).

Physically, the study domain is characterized by high built (building and paved land cover) density in central London near the River Thames and higher vegetation land cover fraction away from the city centre (Figure 1). Overall combined impervious (building and paved) land cover is 45%. Average building heights in the entire domain are around 10 m with areas of high rise buildings in the City of London and Canary Wharf areas with individual building heights up to 310 m.

Vegetation is more abundant outside of the city centre and in several large parks (Figure 1). Overall vegetation land cover (λ_V) fraction in the domain is 51% (25% grass and shrubs <2.0 m and 26% trees above 2.0 m). Most trees (58%) are deciduous species which follow an annual cycle of leaf-on in northern hemisphere spring (April-May) and senescence and leaf-off in autumn (October-November). Overall, water coverage is 3%, with the city bisected West-East by the River Thames and a system of reservoirs in the Northeast quadrant.

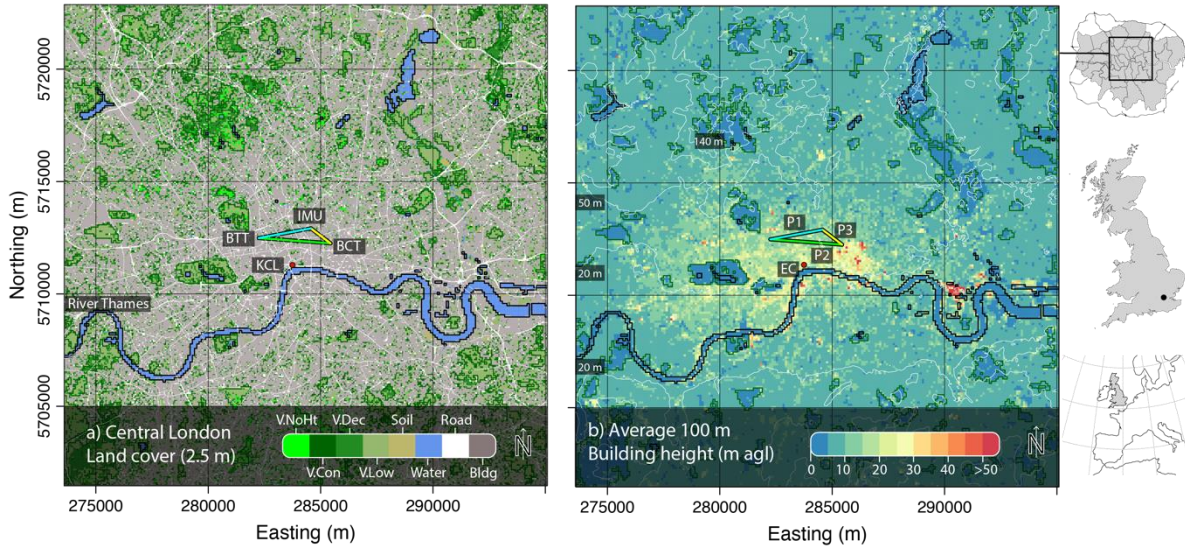


Figure 1. Land cover (2.5 m pixels) and mean building height (100 m pixels) of the study domain with sensible heat flux (Q_H) observation network of scintillometers (lines) and eddy covariance (red circle). The significant water bodies (e.g. River Thames) (black) and extensive vegetated areas (e.g. parks) (green) are outlined. Land cover data are derived from multi-spectral Landsat satellite images (2012) and building heights are from a LiDAR digital surface model (Section 2.5). Land cover categories are ‘V.NoHt’ (vegetation without height information), ‘V.Con’ (coniferous vegetation > 2.0 m height), ‘V.Dec’ (deciduous vegetation > 2.0 m height), ‘V.Low’ (vegetation < 2.0 m height), ‘Soil’, ‘Water’, ‘Road’, and ‘Bldg’ (building). Terrain elevation contours measured during the LiDAR scan are overlaid on (b) (30 m intervals, white lines).

2.2 London measurement network

A unique feature of this study is the availability of an extensive *in situ* measurement network in central London. Observations from the network are used to develop empirical models of r_H , provide inputs to calculate Q_H and turbulent flux source areas, and to evaluate gridded Q_H calculation results (Figure 1).

Turbulent sensible heat flux and radiation measurements are available from the eddy covariance (EC) tower at King’s College London (KCL). The EC instrumentation consists of a CSAT3 (Campbell Scientific, Logan, UT, USA) sonic anemometer and Li-7500 (Li-Cor, Lincoln, NE, USA) open-path gas analyzer mounted at 60.9 m asl (50.3 m agl). Three-dimensional wind velocities, virtual acoustic air temperature, and water vapour mixing ratios are recorded at 10 Hz and flux processing is performed in 30-minute intervals. Detailed description of the EC site and data processing is found in Kotthaus and Grimmond (2014). Incoming ($K\downarrow$) and outgoing ($K\uparrow$) solar radiation, and incoming ($L\downarrow$) and outgoing ($L\uparrow$) longwave radiation are measured at a height of 60.9 m asl (50.3 m agl) (CNR4 net radiometer, Kipp & Zonen).

A network of three scintillometers provide additional observations of area-averaged Q_H in the study domain (Table 1, Figure 1). Scintillometers use path-integrated measurements of perturbations to a beam of infrared light to derive Q_H based on surface layer similarity theory. These instruments provide spatially-integrated measurements from much larger areas than EC. Full description of instrumentation and data processing details for the scintillometer network are found in Crawford et al. (2017).

Satellite overpasses to measure LST occur between 10:52 and 11:02 UTC and calculated Q_H at the overpass times is directly compared with simultaneous measurements from the scintillometers and EC system. To ensure measurements are representative of the satellite overpass time, interpolated values between two 30-minute averaged measurement periods (10:30-11:00 and 11:00-11:30 UTC) are used for comparison.

In general, there is uncertainty in the observed-model comparison due to uncertainties with Q_H observations. Eddy covariance has been shown to have typical hourly uncertainty of 8-10% during daytime periods (Hollinger and Richardson, 2005). This uncertainty comes from a combination of sources including systematic and random sensor errors, vertical flux divergence, and lack of energy balance closure. Scintillometers in complex areas such as central London have typical uncertainty on the order of 20% due to variable meteorological inputs, surface conditions, instrument height, and surface layer similarity theory assumptions (Crawford et al. 2017, Ward 2017).

An additional source of uncertainty in the comparison comes from the use of source area models to weight calculated Q_H surface means (Heidbach et al. 2017). It is generally understood that source area models do not account for complexities in urban areas resulting from flow channelling in the canopy layer or the influence of heat point sources or plumes (e.g. Crawford and Christen 2014). The individual processes contributing to this uncertainty have not yet been quantified rigorously in an urban setting, but previous sensitivity analysis has shown the scintillometer source area

averaged land cover fractions to be insensitive ($<\pm 1\%$) to changes in source area size of -50% to $+20\%$ in central London (Crawford et al. 2017).

There is also uncertainty because radiometer source areas differ from turbulent EC source areas. This is important because r_H is calculated using observed T_R and EC Q_H at KCL (eq. 1). At KCL, the 90% view factor of the radiometer (50.3 m agl) source area extends to a radius approximately 150 m away from the tower (eq. 3 in Schmid et al. 1991). This extent does not include the River Thames (190 m away from the tower), so the River has only a minimal influence on T_R measurements. In contrast, the EC measurements have a different and more dynamic source area (i.e. the location changes, not just solar geometry). At times, more vegetation and water are included in the EC source areas, depending on stability and wind direction (over 50% water land cover during neutral conditions with winds from $175-195^\circ$, Kotthaus and Grimmond 2014, Kent et al. 2017). This means the River may enhance (depress) Q_H during night (day) given the relatively warm (cool) water surface, causing a mismatch between observed $\Delta T (T_R - T_A)$ and Q_H . This uncertainty is expected to be largest overnight when turbulent conditions are weak and the EC source area dimensions extend further to include the river.

Table 1. Scintillometer and eddy covariance network in central London. The effective beam height is the path-weighted mean height of the beam above the surface, including buildings and trees (Crawford et al., 2017).

	P1	P2	P3	EC
Sensor type	Scintec BLS 900	Kipp & Zonen LAS MkII	Kipp & Zonen LAS MkII	Campbell Scientific, Inc. CSAT 3d sonic anemometer
Effective height (m agl)	111.6	140.7	98.7	50.3
Path (P) length (m)	2358	3197	1097	-

2.3 EO-derived LST

Observations from the Enhanced Thematic Mapper Plus (ETM+) and the Thermal Infrared Sensor (TIRS) aboard the Landsat 7 and 8 satellites, respectively, are used to calculate *LST* for 26 individual periods from 7 April 2011 – 26 Aug 2016. All scenes have been acquired between 10:52 and 11:02 UTC and processed using the ATCOR algorithm by the German aerospace centre DLR (DLR 2012, Marconcini et al. 2017). As original ETM+ and TIRS thermal bands are 30 m and 100 m resolution, respectively, all *LST* products were resampled to 100 m spatial resolution. This procedure also includes image corrections for radiometric, atmospheric, and topographic effects and uses a constant surface emissivity value ($\epsilon=0.98$) (see Section 2.5.4 for discussion of uncertainty related to emissivity). Individual pixels are masked during processing from cloud coverage or instrument malfunction impacts. Images are included in this study if pixel retrieval in the study domain is $>60\%$. ETM+ and TIRS sensor field of view is 15° so the viewing angle for individual pixels is within $\pm 7.5^\circ$ off-nadir.

Landsat-8 images have a known problem of banding due to additional stray light from outside the sensor field of view influencing observations (Montanaro 2014). This additional radiation has been shown to enhance *LST* measurements by 1-2 K (in TIRS Band 10). A correction has been developed by Gerace and Montanaro (2017), but this current work was completed before the corrected images became available. However, errors from the stray light problem are considered during uncertainty analysis and results (Section 2.5.4 and Section 3.5-3.6).

2.4 Geospatial surface data

Surface morphology parameters (building height [z_b], z_0 , and z_d) are determined from a high-resolution (1 m) LiDAR-based digital surface model from 2008 (Lindberg and Grimmond, 2011). Morphological variables are calculated for each 100 m pixel and z_0 and z_d vary according to wind direction (every 5°) using methods developed by Kanda et al. (2013) as implemented in the UMEP software package (Kent et al., 2017, Lindberg et al. 2018).

Land cover has been classified at 2.5 m based on multi-temporal resolution satellite imagery (SPOT and WorldView) from 2012 and the LiDAR DSM data (Marconcini et al., 2017). Five land cover categories are defined: buildings (λ_B), paved surfaces (λ_P), water (λ_W), bare soil (λ_S), and vegetation (λ_V). Vegetation is further categorised as low vegetation (<2.0 m), deciduous vegetation (>2.0 m), coniferous vegetation (>2.0 m), and vegetation with no height information. This 2.5 m resolution land cover data are aggregated to 100 m resolution and land cover fractions range from 0-1 for each category.

2.5 Aerodynamic resistance method

2.5.1 Reference height scaling

Gridded geospatial data (z_0 , z_d , λ_V) and atmospheric variables (T_A , u_* , L) are required at the same resolution as *LST* to calculate Q_H using aerodynamic resistance methods. Atmospheric variables, such as wind speed and u_* , are height-dependent and respond to surface characteristics of an upwind fetch that typically extend beyond individual 100 m x 100 m grid cells of *LST* images. Additionally, corresponding surface variables (z_0 , z_d , λ_V) for an elevated atmospheric measurement are representative of a larger source area than individual grid cells.

Given the need for appropriate heights for the atmospheric variables and characterisation of the surface, a reference height for the calculations is defined. In this study, a reference height of $3z_b$ (where z_b is the mean building height) is

selected. Three is chosen to provide a reasonable likelihood of being above the RSL (Roth 1999, Grimmond and Oke 2000, Grimmond et al. 2004, Kastner-Klein et al. 2004) but recognizing the limitation of the depth the urban surface layer (Rotach 1999).

2.5.2 Air temperature and wind fields

Air temperatures from an *in situ* network of meteorological stations are used to generate a T_A field at 100 m resolution. Currently, observations from a single tower-mounted, shielded, and passively ventilated thermometer (Vaisala, Inc., WXT520) at 50.3 m agl are used across the entire domain. Temperatures are height-adjusted in each pixel to a reference height of $3z_b$ (Section 2.4) using an environmental lapse rate of $6.5 \times 10^{-3} \text{ K m}^{-1}$.

During model development, T_A fields were interpolated from distributed networks of air temperature observations (e.g. NetAtmo, WeatherUnderground). However, these datasets introduce additional uncertainty in the current application because of i) uneven spatial distribution of sensors, ii) lack of reliable location metadata for many stations, and iii) lack of evaluation with co-located observations (Gabey et al. 2018). Other T_A measurements in central London are available from the London Urban Meteorological Archive (LUMA), but no consistent set of stations are available for the entire 2011-2016 study period. So, to ensure consistency across the study period, we opted to use a single, high-quality measurement (KCL) as T_A reference at the expense of higher spatial resolution. This procedure introduces some uncertainty because we are unable to resolve phenomena such as urban heat or cool islands (Theeuwes et al. 2015).

This simplification is justified because spatial variability of T_A across the study domain at the reference height ($3z_b$) is expected to be much less than that of LST . This means T_A is essentially spatially constant relative to LST and that spatial variations in LST dominate the $(T_A - LST)$ term in Eq. 1. To further assess uncertainty with T_A , other long-term monitoring stations (e.g. airports) located outside the study domain are also used in Section 2.5.4.

Gridded u and L values are required as inputs to Eqs. 1-2 to determine r_H . Results from a sensitivity analysis (Section 3.5) show that Q_H is relatively insensitive to L , so L is taken from KCL sonic observations and assumed spatially constant across the domain. The gridded u field is determined by the following procedure: Observed wind speed (U), friction velocity (u_*), and Obukhov length (L_{KCL}) are measured by the KCL sonic anemometer ($z_{m, KCL} = 50.3 \text{ m agl}$, approximately $3z_b$ (2012-2016)). The corresponding roughness parameters $Z_{0, KCL}$ and $Z_{d, KCL}$ (Section 2.4) are used in the stability-adjusted (ψ) logarithmic wind profile (using the sign convention of positive ψ as in Stull, 2012):

$$U = \frac{u_*}{k} \left[\ln \left(\frac{z_{m, KCL} - Z_{d, KCL}}{Z_{0, KCL}} \right) + \psi \left(\frac{z_{m, KCL} - Z_{d, KCL}}{L_{KCL}} \right) \right] \quad (6)$$

The measured wind speed is then extrapolated to an arbitrary reference height of 200 m asl (z_{ref} , selected to be frequently well above the RSL and reasonably assume a spatially homogeneous reference wind speed, U_{ref}) assuming vertically constant u_* :

$$U_{ref} = U \frac{\left[\ln \left(\frac{z_{ref} - Z_{d, KCL}}{Z_{0, KCL}} \right) + \psi \left(\frac{z_{ref} - Z_{d, KCL}}{L_{KCL}} \right) \right]}{\left[\ln \left(\frac{z_{m, KCL} - Z_{d, KCL}}{Z_{0, KCL}} \right) + \psi \left(\frac{z_{m, KCL} - Z_{d, KCL}}{L_{KCL}} \right) \right]} \quad (7)$$

The standardised reference wind speed U_{ref} is then applied across the domain and scaled to the $3z_b$ reference height for each grid cell to calculate pixel-specific U' . This uses the roughness parameters estimated for a particular location and assumes spatially consistent stability (i.e. L) across the domain:

$$U' = U_{ref} \frac{\left[\ln \left(\frac{3z_b - Z_d}{Z_0} \right) + \psi \left(\frac{3z_b - Z_d}{L_{KCL}} \right) \right]}{\left[\ln \left(\frac{z_{ref} - Z_{d, KCL}}{Z_{0, KCL}} \right) + \psi \left(\frac{z_{ref} - Z_{d, KCL}}{L_{KCL}} \right) \right]} \quad (8)$$

2.5.3 Aerodynamic resistance parameter

The aerodynamic resistance term (r_H) is calculated (eq. 2) using MOST. It varies both temporally and spatially. In this work, five approaches to calculate r_H are compared (Table 2, also see Appendix Table A.2). Three approaches use empirical relations derived for the central London KCL flux site and two are generalized statistical relations for urban areas based on scale model and urban flux measurements. Additional methods of Jurges (1924), Rowley (1930), and Harman (2004) were also tested preliminarily, however these methods all require a parameterization of high-resolution canopy layer wind speed which is beyond the scope of this work to generate with high confidence.

Table 2. Five methods to determine aerodynamic resistance in central London on a pixel basis.

Method	Method source	Description
R1	This paper	Constant r_H , based on observations at KCL (eq. 1)
R2	This paper	Empirical relation between z_H and solar elevation (δ)
R3	This paper	Empirical relation between z_H and u
R4	Kanda et al. (2007)	Empirical relation between kB^{-1} and Re^* at urban scale model (eq. 4)
R5	Kawai et al. (2009)	Empirical relation between α and land cover in real cities (eq. 8)

2.5.3.1 R1-R3 from central London observations

Three methods rely on findings from KCL tower (central London) observations. These are described from simplest to most complex. The empirical relations are derived using daytime observations ($K_d > 10 \text{ W m}^{-2}$), non-stable ($EC Q_H > 20 \text{ W m}^{-2}$), dry surface conditions (time since precipitation > 12 hours) to correspond to general conditions during satellite image acquisition. The observation results for these methods are in Section 3.2-3.3.

The R1 method uses r_H calculated from Eq. 1 and observed Q_H , T_A , and substituting radiometric surface temperature (T_R) for T_0 . The T_R is calculated using the Stefan-Boltzmann equation with observed longwave radiation upward and downward components and an assumed bulk emissivity of 0.95 for an urban setting (Arnfield 1982, Kawai et al. 2009, Kotthaus et al. 2014). In general, there is uncertainty in using T_R as a proxy for T_0 arising from i) the choice of emissivity value, ii) lack of atmospheric correction, iii) source area differences between the radiometer and eddy covariance instruments, and iv) radiometer view bias.

The mean r_H value of 40 s m^{-1} for all periods in 2015 for 10:30-11:30 UTC is used (approximate time of satellite overpass) for all images. This is a simple approximation that assumes spatially constant r_H and does not account for variations in atmospheric conditions (u^* , L) nor surface land cover and roughness spatial variations.

The R2 method calculates z_H based on an empirical relation between solar elevation (δ , ° above horizon) and z_H observed at the central London eddy covariance tower (Section 3.3). The z_H is found by first solving for r_H using Eq. 1 and then solving for z_H in Eq. 2, using available tower-based (50.3 m agl) meteorological observations (u^* , L , T_A), surface parameters (z_0 and z_d) calculated in 10° wind direction increments (Kanda et al. 2013, Crawford et al. 2017), and substituting radiometric surface temperature (T_R) for T_0 . Solar elevation is calculated for the day of year and time of each overpass (Meeus 1991, NOAA 2017).

The R3 method uses z_H determined from a linear relation between mean wind speed (U) and z_H observed at the KCL tower (Section 3.3). The z_H is calculated as described for R2 and wind speed varies spatially (Section 2.5.2) depending on surface roughness (Section 2.4) and reference height (Section 2.1).

For R2-R3, the r_H value is calculated for each pixel using Eq. 2 once z_H has been determined. The stability function for heat (ψ_h) used for unstable conditions in Eq. 2 is (van Ulden and Holtslag, 1985):

$$\psi_h = 2 \ln \left(\frac{1+x^2}{2} \right) \quad (9)$$

where (Högström, 1988):

$$x = 0.95 \left[1 - 15.2 \left(\frac{z'}{L} \right) \right]^{0.5} \quad (10)$$

where $z' = z_m - z_d$ and z_m is the measurement height.

The u^* and L values in Eq. 2 are assumed spatially constant and set to observed values at KCL. This simplification is necessary to make the problem more tractable, though the assumption of spatial homogeneity is likely not physically realistic across this study domain and artificially decouples Q_H from spatial variations in L and u^* (e.g. Su 2002). Our approach instead is to quantify uncertainty resulting from this simplification (Section 3.5).

During model development, an iterative approach using linked, spatially dynamic u^* , L , and Q_H values was explored. However, u^* and L values were not well-constrained and this iterative procedure resulted in greater model uncertainty and poorer comparison to observations than the simpler approach. Overall, Q_H results are found to be relatively insensitive to variations in L and more sensitive to u^* (Section 3.5).

2.5.3.2 Literature based methods (R4-R5)

Empirical relations from observations at KCL (R1-R3) are compared to established methods described in the urban climate literature. The R4 method uses Kanda et al.'s (2007) 'urban' α parameter (1.29) for Eq. 4 based on observations over the COSMO urban scale model in Japan (Figure 2). The difference from the α value used for rough-bluff natural surfaces (2.46) is attributed to differences in mean flow regimes and different surface roughness of the urban model compared to bluff natural surfaces (Kanda et al. 2007). It is important to note that i) the COSMO model has neither vegetation nor anthropogenic heat (Q_F) sources (both will influence kB^{-1} and observed Q_H values) and ii) the original R4 model formulation is designed for non-vegetated urban surfaces. Therefore, R4 results are expected to differ from R1-R3 (empirical models tuned for this specific site). R4 inclusion is intended as a relevant benchmark; therefore, 'Observed - R4' differences provide potential constraints on the influence of Q_F and vegetation.

During implementation, Re^* is determined based on u^* and z_0 for each pixel. For pixels in the London domain with water or vegetation land cover fractions > 0.8 , the α value is set to 2.46 of 'natural' rough-bluff surfaces.

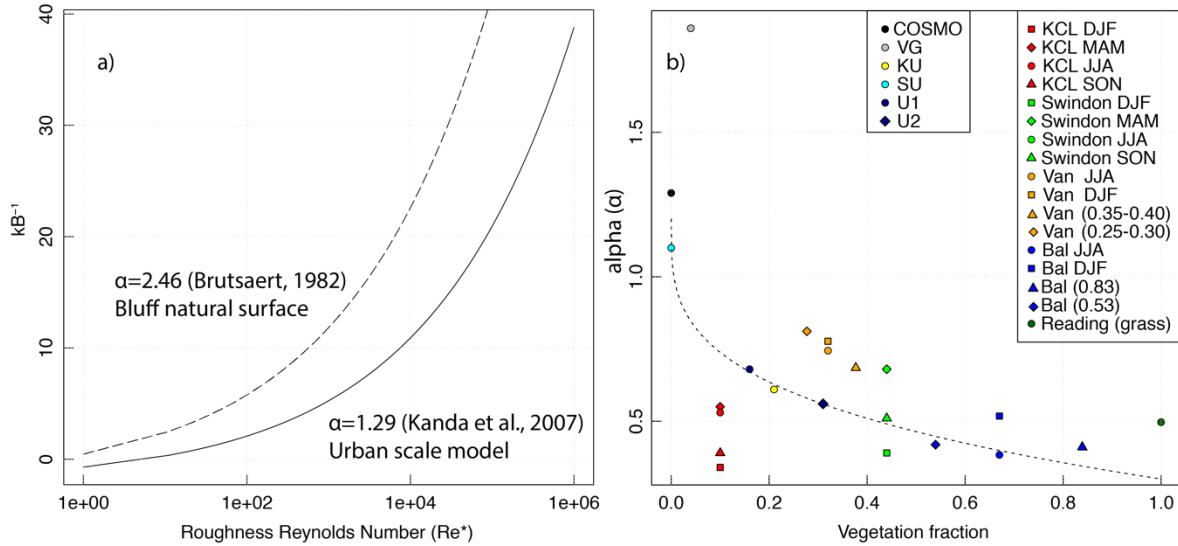


Figure 2. Statistical relations from a) physical urban scale model (COSMO, Kanda et al., 2007) and b) local-scale urban observation sites (Kawai et al. 2009) used to calculate the aerodynamic resistance term (r_H). For b) ‘COSMO’ scale model (Kanda et al. 2007), Vancouver-light industrial (‘VG’, Voogt and Grimmond 2000), Tokyo Kugahara (‘KU’, Moriwaki and Kanda 2006), Tokyo business district (‘SU’, Sugawara 2001), Basel-Sperrstrasse (‘U1’), and Basel-Spalenring (‘U2’) (Christen and Vogt, 2004) are those used by Kawai et al. (2009). Results from central London (‘KCL’, Kotthaus and Grimmond 2014), Swindon (Ward et al., 2013), Vancouver-Sunset (‘Van-ST’, Crawford and Christen, 2015), Baltimore (‘Bal’, Crawford et al. 2011), and University of Reading reference grass site (‘Reading’) are added in this work. These sites are shown for contrasting meteorological seasons (DJF, MAM, JJA, SON), and average summertime vegetation land cover fractions.

The R5 method allows r_H to vary spatially with changes in vegetation land cover (λ_v) as proposed by Kawai *et al.* (2009) (Figure 2b). The original findings use data from five local-scale urban EC measurement campaigns with a vegetated land cover fraction range of 0-0.3. The α value in Eq. 4 is found to decrease as vegetation land cover fraction increases:

$$\alpha = a_u - (a_u - a_L) * \lambda_v^b \quad (11)$$

where a_u (1.2) and b (0.29) are empirical coefficients and a_L is set to 0.3 based on α found experimentally in completely vegetated ecosystems. The R5 method permits the urban fraction within grids of numerical weather prediction to vary. The application here is an extension beyond the original purpose to determine if i) the observed relation holds for vegetation land cover fraction values greater than 0.3 and ii) whether this can be applied at higher resolutions and evaluated against measurements in real cities.

Here, the urban vegetation land cover range is expanded to 0-0.8 by adding four additional sites: Vancouver-Sunset, Canada (Crawford and Christen, 2015); London-KCL, UK (Kotthaus and Grimmond, 2014); Swindon, UK (Ward et al. 2013); and Baltimore, USA (Crawford et al. 2011).

For each site, the α value is found by rearranging Eqs. 1-2 to solve for kB^{-1} and then plotting kB^{-1} against observed Re^* . At each site, meteorological variables (u^* , L , T_A) are observed, T_R is calculated and used as a substitute for T_0 (Section 2.5.1), and surface parameters (z_0 and z_d) are determined for 20° wind sectors using anemometric methods in neutrally stable conditions (Grimmond and Oke, 1999). Additionally, data are stratified by season (DJF, MAM, JJA, SON) to assess variability from changing canopy and weather conditions and by wind sector (for Baltimore and Vancouver-Sunset) to distinguish between source areas with contrasting vegetation land cover fractions.

The overall trend described by Kawai *et al.* (2009) is supported by the additional observations (Figure 2b), though there is scatter about the trend line (mean absolute deviation = ± 0.18). A physical explanation for this trend is that momentum transfer is enhanced relative to heat transfer due to increased pressure drag from dominance of bluff bodies in less vegetated urban environments. This increases α , thus also kB^{-1} and r_H values. As vegetated land cover fraction increases, the canopy becomes more porous, pressure drag is reduced, and heat transfer efficiency is enhanced by the intricate vegetation canopy 3D surface. Values for α determined experimentally for rough, porous vegetated canopies such as pine forest and savannah scrub are approximately 0.3 (Kawai et al. 2009 and references therein).

London-KCL appears as an outlier in this figure with lower α values than expected (0.45) based on vegetation fraction (0.09). A possible explanation for this could be that closely packed buildings in central London place this site more towards the skimming flow regime where form drag from bluff buildings is diminished. Another explanation is the influence of the River Thames on EC measurements and differing source areas between T_R (radiometer) and Q_H (EC) used to derive r_H , kB^{-1} , and α (Section 2.2).

To implement R5, pixel-specific α is derived using λ_v and Eq. 11. Then kB^{-1} is calculated using Eq. 4. For water or vegetation land cover fractions >0.8 , the α value is set to 2.46 of ‘natural’ rough surfaces.

2.5.4 Quantifying uncertainty

To quantify model uncertainty, a modified Monte Carlo approach is used to sample the parameter space of input meteorological and surface variables. The model is run with 20 unique sets of inputs within a prescribed range from the original observed or calculated value (Table 3). Values within this range are generated using quasi-random numbers. For each run, each variable is sampled at a unique location in the allowed range. The quasi-random numbers are generated assuming a uniform distribution and this conceptually represents a systematic bias which affects all individual grid cells (i.e. individual grid cell uncertainties are not independent).

The range for each variable was determined using a variety of approaches. For *LST*, we consider three independent sources of error: surface emissivity (ε), sensor bias, and satellite view bias. For ε , the uncertainty interval is determined by calculating T_R from KCL radiometer measurements with bulk emissivity set to 0.9 and 1.0 as physically reasonable upper and lower constraints. The resulting sensitivity of T_R to this ε range is on average 1.2 K (± 0.6 K) for all hours at 11:00 UTC from 2012-2016. The KCL T_R during each overpass (with $\varepsilon=0.98$) is compared directly to extracted *LST* values (weighted mean of pixels surrounding the KCL tower to approximate the radiometer source area) and *LST* is on average 0.8 K higher than T_R . This is comparable to the *LST* bias (0.67 K) found between application of constant and variable emissivity values to multispectral satellite images in an urban area (Mitraka et al. 2012).

The sensor bias is the reported average absolute error estimate due to the stray light problem (+1 to +2 K) (Gerace and Montanaro 2017). For satellite view bias, *LST* is likely underestimated relative to the complete surface temperature by 0 to -2.5 K at 11:00 UTC (which acts to offset the stray light sensor bias), if we assume a nadir viewing angle. This is based on thermal camera measurements in an urban neighbourhood (Adderley and Christen 2015) and a physical scale urban model (Roberts 2010) that found maximum differences between nadir and complete surface temperatures at solar noon (2.2-2.5 K) and near-zero difference at 10:30 local time (Adderley and Christen 2015). This error is expected to vary spatially and generally increase with building height and canyon aspect ratio as the proportion of walls to the total 3D urban surface area changes (Krayenhoff and Voogt, 2016). Additional errors result from the actual off-nadir view angle ($\pm 7.5^\circ$), satellite azimuth angle, and thermal anisotropy of the surface. There are likely further sources of error in *LST* observations, such as neglecting urban aerosols during atmospheric correction, that are not quantified.

For T_A , the uncertainty range is the mean difference between KCL and Heathrow airport on the outskirts of central London for 10:30-11:30 UTC; this is taken to be the likely maximum air temperature difference within the spatial domain during the overpass times. For wind speed, the average difference between predicted wind speeds using the methods described in Section 2.5 and actual measurements from two stations in the London network (BCT, IMU) are used. For z_0 and z_d , the range is based on analysis of several morphometric and anemometer-based methods to determine their values in central London (Kent et al. 2017). For α in Eq. 9, the value is the mean absolute difference between the fit model curve and observation points in Figure 2b. The ranges of u^* and L are set to the standard deviation of measurements at the KCL flux tower at 10:30-11:30 UTC during an entire year (2016), essentially substituting observed temporal variability for spatial variability. The solar elevation uncertainty is based on variations in overpass time (10:52-11:02 UTC) and from simplified orbital calculations.

Vegetation fraction uncertainty is set to the 100 m pixel difference (± 0.1 , includes 95% of 100 m pixels) between land cover determined for this project and that from the UK Ordnance Survey MasterMap (Ordnance Survey 2017) in a subset of the modelling domain. For elevation, uncertainty is estimated from a comparison between LiDAR-derived elevation datasets from 2008 and 2015 for a spatial subset where there is overlap between the datasets. LiDAR instrumentation errors are $< \pm 1$ m and uncertainty primarily is from changes due to building construction. Between 2008 and 2015, 99% of 100 m pixels are within ± 4 m elevation difference (though roughness element heights are on average 0.5 m taller in 2015 compared to 2008).

It should be noted that there are likely other sources of uncertainty in individual pixels resulting from process that have not been quantified. For example, complexities related to sub-pixel heterogeneity are not considered explicitly and advection from cool grid cells (e.g. parks, rivers) to warmer adjacent pixels could enhance micro-scale sensible heat fluxes by increasing micro-scale vertical temperature gradients.

Table 3. Input variables to calculate Q_H and their estimated uncertainty range used for the Monte Carlo and sensitivity analyses.

Variable	Description	Estimated uncertainty range (\pm)	How uncertainty range is determined
<i>LST</i>	EO-observed from Landsat-8 satellite based on thermal infrared radiation	2 K	Combined uncertainty from: i) surface emissivity, ii) sensor bias, iii) view-angle bias.
T_A	Air temperature spatially interpolated from observation network	0.5 K	Mean difference between central London and Heathrow airport at 11:00 UTC.
U	Reference mean wind speed observed at KCL tower, spatially calculated using log law	3 m s ⁻¹	Mean difference between predicted and observed values at 2 stations in central London.
u^*	Friction velocity observed at KCL tower, assumed spatially constant	0.15 m s ⁻¹	IQR of measured values for a full year at KCL at 11:00 UTC
z_d	Displacement height calculated from DSM using Kanda et al. (2013) method, varies by wind direction	10 m	Based on analysis of morphometric and anemometer-based approaches in central London (Kent et al. 2017)

z_0	Roughness length calculated from DSM using Kanda et al. (2013) method, varies by wind direction	2 m	Based on analysis of morphometric and anemometer-based approaches in central London (Kent et al. 2017)
z	Reference height determined LiDAR observed DSM from 2008	4 m	Comparison between 2008 and 2015 LiDAR elevation datasets.
L	Obukhov Length observed at KCL tower, assumed spatially constant	300 m	IQR of measured values for a full year at KCL at 11:00 UTC
λ_v	Vegetation land cover fraction from remote sensing	0.1	Estimate based on comparison between two land cover datasets.
α	Alpha value in Eqs. 4 and 8 to calculate kB^{-1}	0.18	Mean absolute deviation of observed values about the model curve in Figure 2b.
δ	Solar elevation angle	3°	Based on variations in overpass time and reference time of 11:00 UTC and orbital simplifications in solar model.

Thus 20 ensemble members are generated for each pixel and each method, for each LST image. The uncertainty range for each method is estimated from the median absolute difference between the 10% and 90%^{ile} Q_H values calculated for each pixel. The median value of this matrix is then interpreted as the average uncertainty range for each method across the spatial domain (both absolute $W\ m^{-2}$ and relative to median Q_H for all images).

3 Results

3.1 EO-derived LST

Median LST in the study domain derived from EO measurements follows an expected annual course with highest values in summer and lowest in winter (Figure 3a). The median LST values for each scene are generally higher than the T_R range (5th-95th %^{ile}) observed at KCL from 2012-2016 because the EO scenes are from cloud-free periods and do not include overcast and rainy times. LST values are also all warmer than air temperatures, implying unstable atmospheric conditions and positive Q_H .

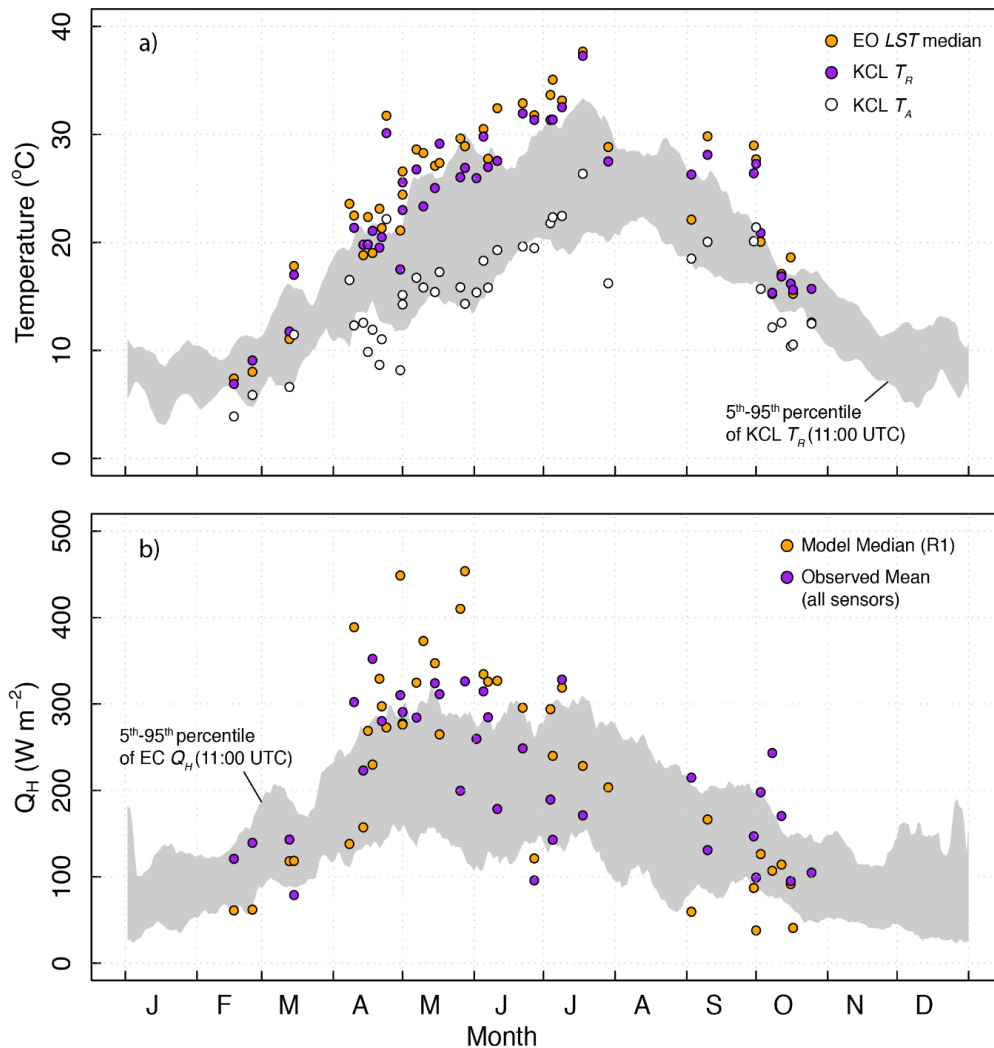


Figure 3. Annual course of a) EO-derived LST , tower-observed radiometric temperature (T_R) and air temperature (T_A) and b) tower-observed and modelled Q_H (R1). Observed T_R and T_A in a) and observed and modelled Q_H in b) are at the same time as each LST overpass. The 5th-95th %^{ile} ranges of observed T_R values (grey shading) is shown for all days from 2012-2016 at 11:00 UTC with a 10-day smoothing filter. For observed T_R (a), the range of values includes emissivity variations from 0.90-1.0. For Q_H (b), observed values are from the three scintillometers and EC system (Figure 1).

Spatially, coolest temperatures are generally found in more vegetated areas and for the surface of water bodies. LST tends to increase with higher building land cover fraction (λ_B) (Figure 4a). The greatest rate of increase in LST is when λ_B ranges from 0-0.5, above which LST remains constant (5-7% above spatial mean). In winter, LST is relatively high (10% above mean) in areas with high building fractions (>0.8), possibly due to anthropogenic heating, however there are few data points from winter ($n=2$). In this analysis, pixel LST is normalized relative to the spatial mean ($\langle LST \rangle$) for each scene ($LST/\langle LST \rangle$) and only pixels with water land cover fractions <0.5 are used. The normalized LST pixels are binned in land cover fraction increments of 0.1. The relation between vegetation land cover and LST is the inverse (not shown), i.e. LST decreases as vegetation fraction increases.

Though LST increases as building land cover increases, measured LST tends to be cooler in areas with tall buildings (Figure 4b). Pixels with tallest buildings (>120 m on average) are in general 10% cooler than the spatial average. In this analysis, only pixels with vegetation and water land cover fractions <0.5 are selected and normalized LST pixels are binned in 10 m building height increments.

This cooling trend is evident for various classes of building land cover fractions. For example, LST is relatively low when $\lambda_B < 0.2$, yet LST still decreases as mean building height increases. Another notable trend is that when buildings are shorter (<80 m), LST increases with increasing λ_B , consistent with Figure 4a. However, when buildings are taller (>110 m), this pattern reverses and LST tends to decrease with λ_B .

When buildings are shorter, the positive correlation between LST and λ_B can intuitively be explained due to the greater fraction of buildings and their rooftops at the expense of cooler grass and tree vegetation, with a satellite view bias towards warm rooftops (at the 11:00 UTC overpass time). In the tall building regime, the apparent cooling as building density increases could result from several explanations: i) increased surface shading and reduced sky view factor from tall buildings, ii) increased proportion of shaded walls that are included in off-nadir satellite view, iii) reduced emissivity of building materials such as glass and steel present in higher proportions in areas with tallest buildings.

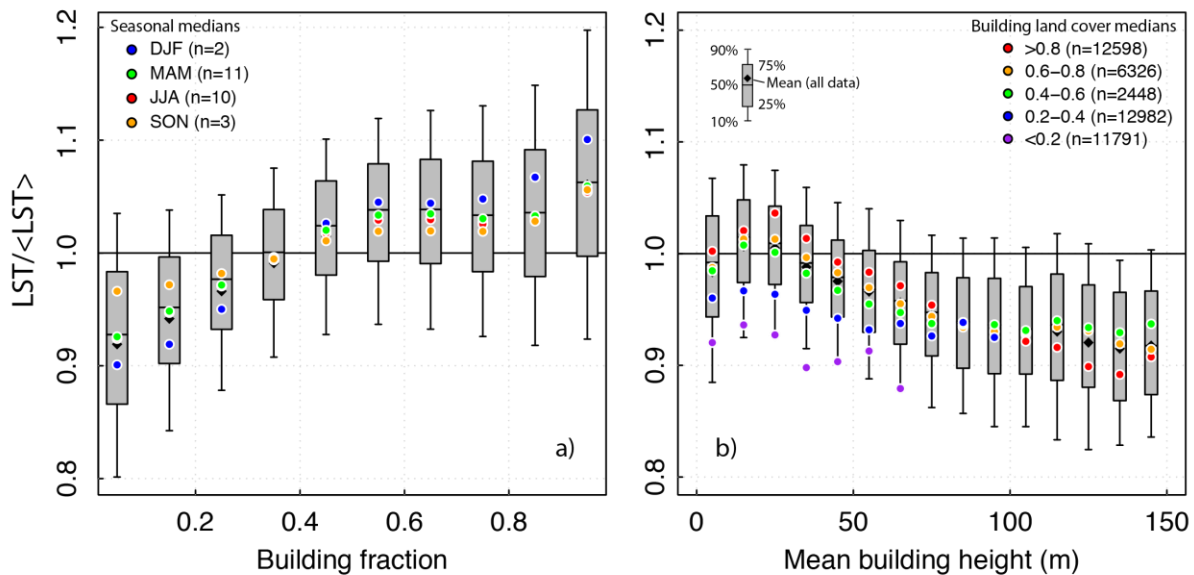


Figure 4. Normalized LST for all available Landsat images binned by a) building land cover fraction with medians for meteorological season (coloured dots) and b) mean building height with medians for building land cover fraction (coloured dots). In a) only pixels with water <0.5 are used and in b) only pixels with vegetation and water <0.5 are selected.

Four images from contrasting periods (summer day, summer night, winter day, and winter night) are chosen as representative examples for comparison. Based on these images, daytime LST has higher spatial variance (s.d.=2.67 K on 8 June 2013 11:00 UTC) whereas nighttime LST is more uniform (s.d.=0.12 on 8 June 2011 21:43 UTC) (Figure 5). During winter (not shown), daytime variability is less than in summer (s.d.=1.08 K on 16 Feb 2016), though nighttime variability between seasons is similar (s.d.=0.13 K on 25 Dec 2011 21:44 UTC).

LST patterns also exhibit spatial structure correlated with vegetation and building land cover fraction. Variograms for the four contrasting periods show spatial autocorrelation across a range of spatial scales (Figure 6). Low variance is associated with homogenous surfaces and high variance with heterogeneity.

Summer daytime has highest variance at all scales, while summer and winter nights have the lowest. For all images however, variance increases up to 500 m where there is an inflection and the variance curve becomes relatively flat. This implies the spatial surface temperature structures are more homogenous (i.e. less variance) at length scales less than 500 m. In contrast, a field of uniformly distributed random numbers has a flat variance curve across the entire range of length scales. Vegetation and building land cover fractions also exhibit an inflection at around 500 m, suggesting observed LST patterns are linked to the built and vegetated structure in the area.

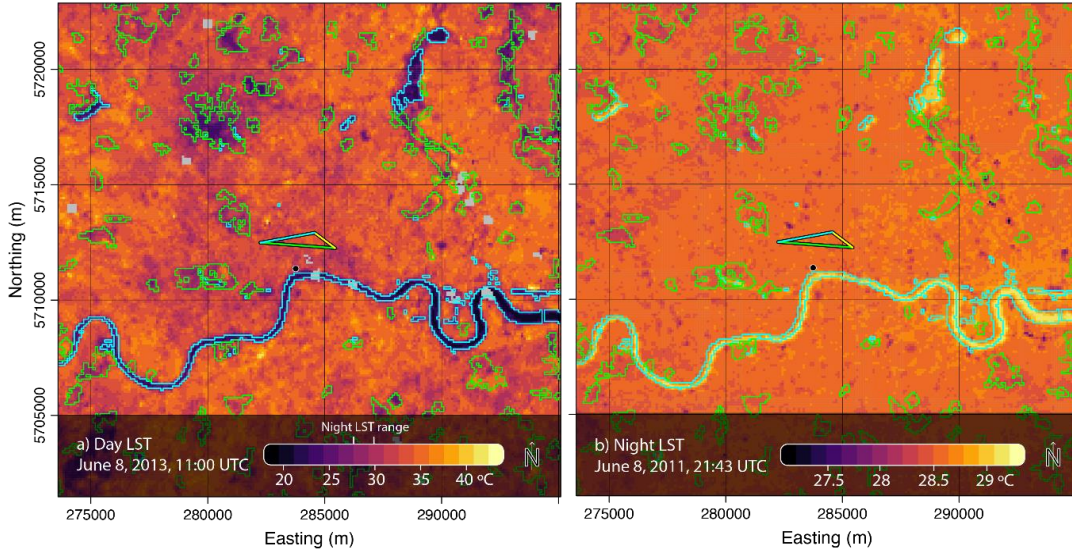


Figure 5. Summer EO-derived LST for representative a) day and b) night periods. Daytime images are from Landsat satellite and nighttime images are from the ASTER satellite. Parks (green), water bodies (blue), and the central London Q_H observation network are also shown (coloured lines and black circle).

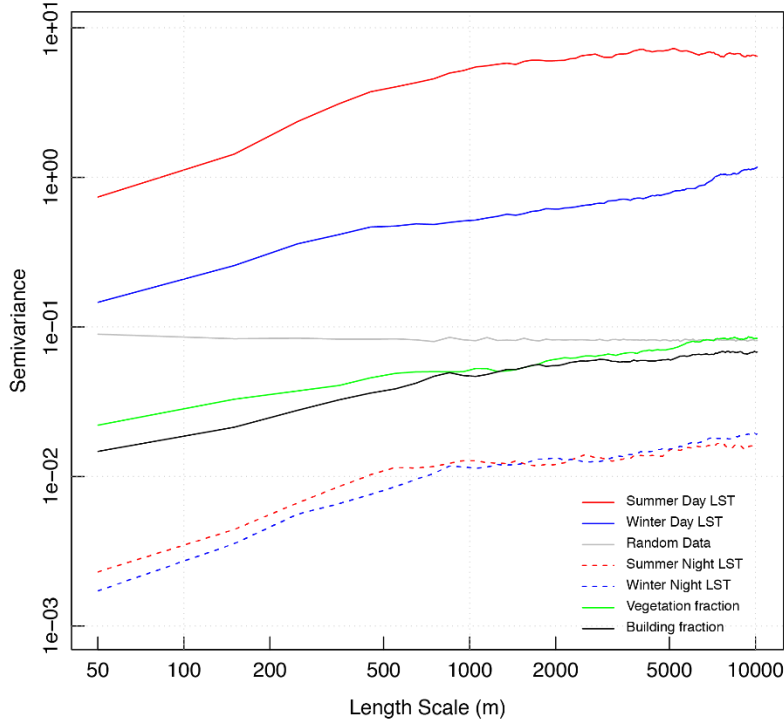


Figure 6. Variogram of LST from four contrasting time periods. A field of uniformly distributed random data is shown for comparison. Both axes are logarithmic.

3.2 Temporal variability of r_H

To assess temporal variability of r_H and variables used to calculate r_H , we use continuous observations from the KCL EC tower for a full year (2015). Observed Q_H and ΔT ($T_R - T_A$) follow expected diurnal and seasonal courses, with highest values during spring-summer (MAM-JJA) and midday periods and lowest values during winter (DJF) and overnight (Figure 7a-b). Q_H tends to be highest during spring (MAM, $>200 \text{ W m}^{-2}$ from 1100-1500 h), though ΔT is highest during summer ($>8^\circ\text{C}$ from 1000-1300 h). This is consistent with prior observations at this site that found highest Q_H in springtime when there is relatively plentiful energy input from Q^* , but vegetation evapotranspiration is not yet at full strength to partition energy towards Q_E (Kotthaus and Grimmond 2014). For Figure 7a-f, daytime ($K\downarrow > 10 \text{ W m}^{-2}$) data from unstable periods ($Q_H > 20 \text{ W m}^{-2}$) with a dry surface (time since rain $> 12 \text{ h}$) in 2015 are used.

The thermal resistance (r_H) calculated (Eq. 1) at KCL for all hours in 2015 using measurements of Q_H , T_A , and T_R ($\varepsilon=0.95$) has a clear diurnal pattern (Figure 7c). The highest median r_H values occur during midday (36.9 s m^{-1} from 1000-1400 h) and lowest overnight (median, 10.0 s m^{-1} from 2100-0500 h). There is considerable variability (mean of the s.d. for all binned hours is 52.4 s m^{-1}). Seasonally, median values are highest in summer (peak at 55.6 s m^{-1} at 1100 h) and lowest during winter (peak 23.1 s m^{-1} at 1200 h). Seasonal differences in r_H are likely due to a combination of seasonal

differences in vegetation canopy state and anthropogenic heat flux (Q_F). Constant r_H at 10:30-11:30 (40 s m^{-1}) is used for the R1 method to model r_H (Section 2.5).

It is somewhat counterintuitive that r_H is largest during the day, when Q_H and ΔT are highest. This differs from the diurnal pattern when r_H is modelled directly using MOST (Eq. 2) with kB^{-1} from eq. 4 (α set to 0.45, Figure 2b). The modelled diurnal cycle shows r_H is lowest during midday when Q_H and u^* are highest, and highest overnight (also see Appendix 1 Figure A1, Table A2). During daytime, modelled and ‘observed’ r_H values are comparable, however, differences occur overnight (up to 30 s m^{-1}). A reason for this discrepancy could be due to source area differences between the radiometer and turbulent EC source areas at KCL, particularly overnight (Section 2.2). Though this undoubtedly introduces uncertainty to estimates of r_H from measurements at KCL, the same diurnal pattern of r_H as Figure 7 is also found when using both i) Q_H from the P2 scintillometer to solve for r_H (along with T_A from IMU and T_R from KCL), which is affected much less by the river and ii) EC Q_H filtered by wind direction ($300^\circ - 45^\circ$) to avoid the river’s influence. Additionally, there is overall greater uncertainty during nighttime both because EC measurements have greater uncertainty due to less vigorous vertical mixing and MOST assumptions begin to break down (e.g. Best and Grimmond 2015).

Magnitudes of r_H observed at the KCL tower are slightly higher than observed from the scintillometer source areas. The scintillometer r_H is estimated using observed Q_H , T_A , and scintillometer source area-weighted LST in Eq. 2. Mean values for satellite overpass times range from $32.6 - 39.2 \text{ s m}^{-1}$ (-18.5% to -2.0% difference from KCL). Differences are likely due to land cover and urban form differences between scintillometer and EC source areas, differences between LST and T_R , and from satellite overpass bias towards clear-sky conditions.

The same diurnal and seasonal cycles as r_H are evident in hourly median kB^{-1} values for 2015 at KCL (Figure 7d). The kB^{-1} term is calculated using Eq. 2 with r_H determined from observations (Eq. 1), measurements from KCL (u^* , L), and z_0 and z_d calculated for 10° wind sectors using the Kanda et al. (2013) method (Section 2). Physically, this can be interpreted as enhanced momentum transfer relative to heat transfer during midday. Momentum transfer is enhanced by form drag in urban areas, while heat transfer is influenced more by molecular diffusion near the surface and thus tends to encounter greater aerodynamic resistance (Kanda et al. 2007). This interpretation is also supported by observation of higher u^* and lower z_H values during afternoon. We have higher confidence in these diurnal patterns of kB^{-1} and z_H than in r_H because they generally agree with modelled diurnal cycles using Eqs. 3-4 (though the modelled range of values is much smaller than measurement-derived values).

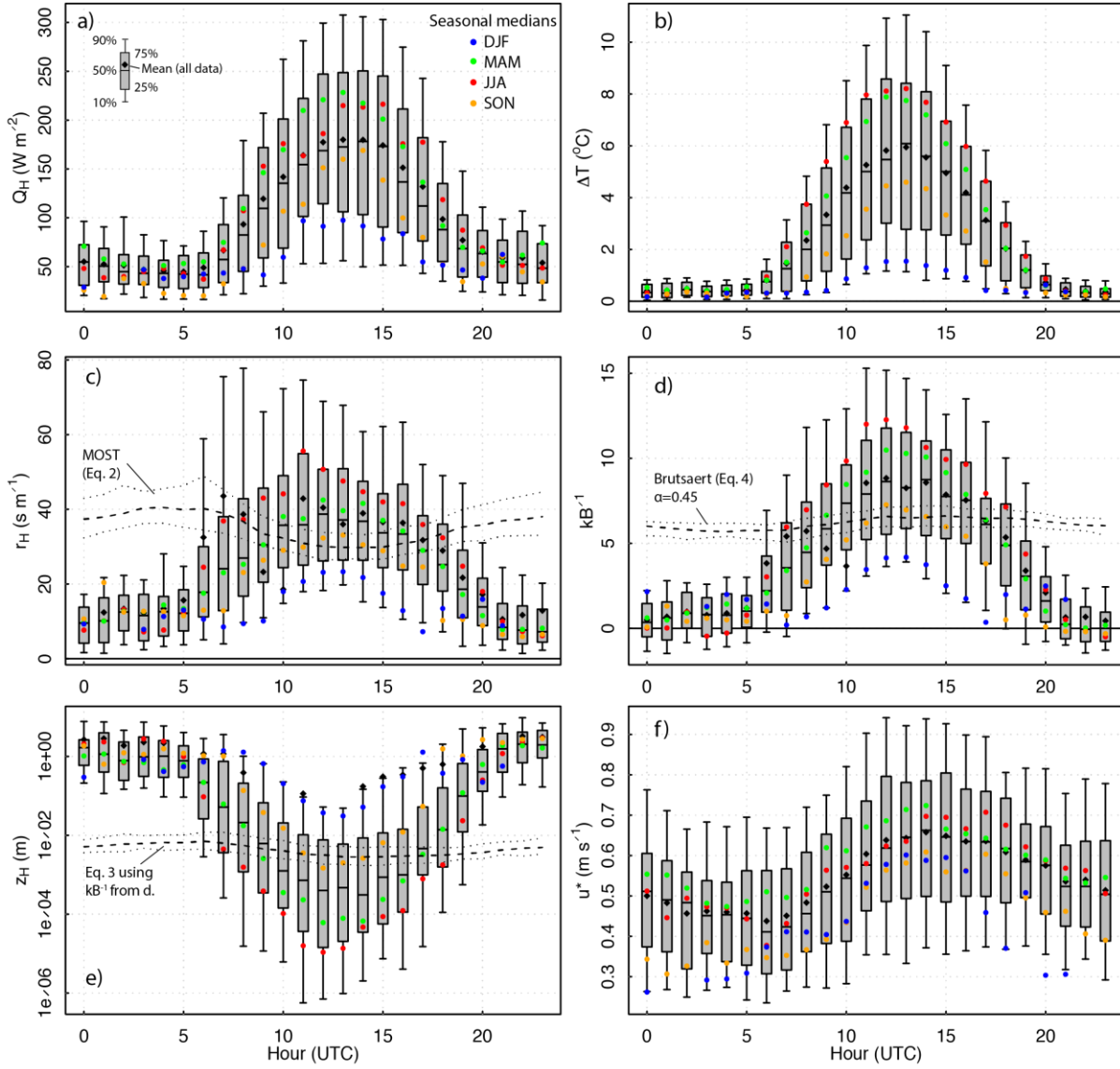


Figure 7. Diurnal course of hourly a) EC Q_H , b) T_R-T_A , c) r_H , d) k_B^{-1} , e) z_H , and f) u^* from KCL measurements during 2015 or calculated using Eq. 2-3. Seasonal (DJF, MAM, JJA, SON) medians (coloured dots) are shown within the boxplot which are based on all 2015 data. Note e) y-axis scale is logarithmic. For c-e), boxplots and dots are derived from KCL measurements and are compared to hourly median (dashed line) and IQR (dotted line) results from the other methods (Appendix 1 Figure A1, Table A2).

3.3 Temporal variability of z_H

Median hourly z_H values are small throughout the day but vary across several orders of magnitude (Figures 7e, 8). Here, z_H is calculated using Eq. 3, based on k_B^{-1} determined from observations (Eq. 2, using r_H calculated from measurements [Eq. 1]), with z_0 calculated for 10° wind sectors using the Kanda et al. (2013) method (Section 2). The diurnal cycle of z_H in Figure 7e generally agrees with that calculated using Eqs. 3 and 4 (though this range of values is much smaller). Highest values are found overnight (up to 2.9 m at 00:00 h) and lowest during midday (1.3×10^{-4} m at 12:00 h).

In central London, z_H is found to vary with solar angle above the horizon, consistent with results from Vancouver (Voogt and Grimmond 2000), but in contrast to findings over the COSMO scale model (Kanda et al. 2007). There is a possibility of a spurious correlation between solar angle and z_H due to turbulence, which also is expected to vary with solar angle. However, we find similar patterns during both neutral ($-0.1 < z'/L < 0.1$) and unstable ($z'/L < -0.1$) conditions. This relation is the basis for method R2 (Section 2.5).

We also find z_H varies with wind speed (R3, Section 2.5), turbulence (standard deviation of 10 Hz vertical wind speed, σ_w , measured by the KCL sonic anemometer), and stability (z'/L). As mean wind speed and σ_w increase, z_H tends to decrease and median z_H is lower (higher) during unstable (neutral) conditions (Figure 8). Here, only daytime ($K \downarrow > 10 \text{ W m}^{-2}$), non-stable ($Q_H > 20 \text{ W m}^{-2}$), dry surface conditions (time since rain > 12 h) are analysed to avoid uncertainties during overnight, reduced mixing periods.

These observations can be explained conceptually by analogy with a surface boundary layer. By definition, z_H is the height at which $T_0 = T_A$. When there are unstable conditions and vigorous turbulence, cool air is mixed downwards into the thin layer between the surface and z_H . This acts to lower z_H , and overall heat transfer is enhanced by turbulent transport

above z_H . In contrast, during neutral or stable conditions with minimal turbulence, the z_H height grows as Q_H from the surface acts to warm the air in contact with the surface via molecular diffusion.

This is somewhat contradicted however by the observed relation between increasing surface bulk heat transfer coefficient (C_H) and increasing z_H , calculated (Kanda et al. 2007):

$$C_H = \frac{Q_H}{\rho c_p U (T_R - T_A)} = \frac{1}{r_h U} \quad (12)$$

A possible explanation for this trend is related to the different source areas influencing radiometers and turbulent EC measurements (as indicated for r_h in Figure 7).

Overall, it remains difficult to interpret the large diurnal variations in z_H and their physical basis. These variations could be an artefact of the measurements used to derive z_H . For example, the apparent relation between z_H and solar angle may be due to differences in LST and the effective surface temperature (T_E). According to Kanda (2005), T_E is the operative driver of Q_H and is formulated as the average of individual facets' surface temperatures weighted by a local bulk transfer coefficient. Differences between T_E and practical substitutes such as T_R or LST used in Eq. 1 vary diurnally according to solar angle and resulting thermal anisotropy of the 3d urban surface and are thus manifested in derived z_H . In general, targeted, controlled experiments may offer a more suitable approach for more in-depth investigation of z_H . However, this requires more detailed surface temperature measurements than can be obtained currently by EO and is the driver behind other ongoing work (e.g. Morrison et al. 2018).

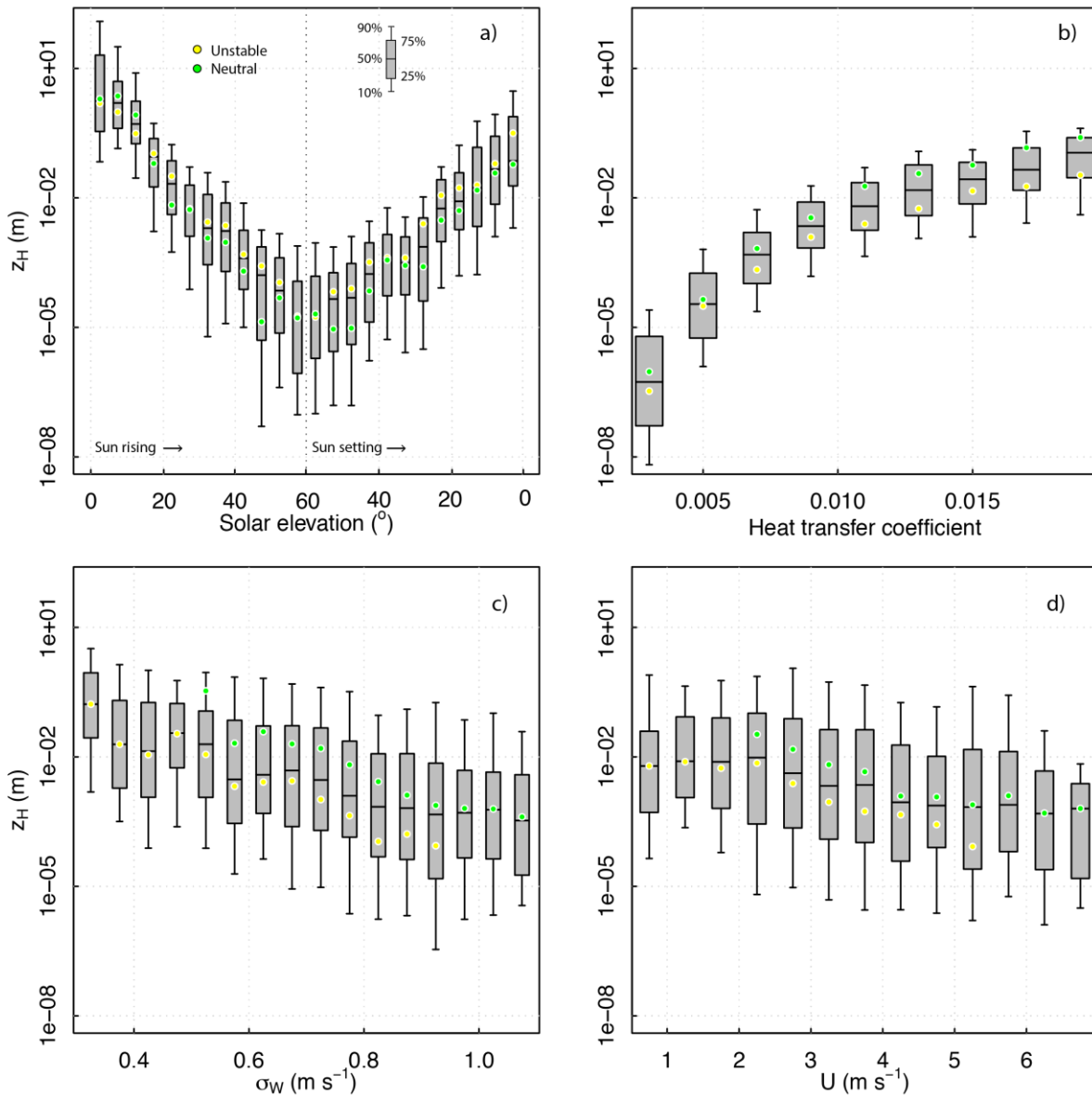


Figure 4. Normalized LST for all available Landsat images binned by a) building land cover fraction with medians for meteorological season (coloured dots) and b) mean building height with medians for building land cover fraction (coloured dots). In a) only pixels with water < 0.5 are used and in b) only pixels with vegetation and water < 0.5 are selected.

3.4 Influence of Q_F

Another factor affecting *in situ* observations with implications for the ARM method is the influence of Q_F . It is well-known that scintillometers and EC Q_H observations in cities also include a portion of Q_F (e.g. Crawford et al. 2017). Modelling work in central London suggests that between 2/3 (Bohnenstengel et al. 2014) and 80% (Iamarino et al. 2012) of Q_F is expressed as Q_H , with the remainder partitioned towards $L\uparrow$, latent heat flux (Q_E), storage heat flux (ΔQ_S), and waste water. This contribution will vary by time of day, day of week, and season according to local energy consumption for space heating, vehicle transportation, and lighting, etc.

In terms of the ARM approach, the overall effect of Q_F is complex. Direct Q_F emissions to the atmosphere (e.g. from vehicle exhaust or building chimneys) will warm the atmosphere as a function of the urban boundary layer (UBL) height (with dynamic feedback) and Q_F input. A simple calculation assuming a well-mixed UBL shows that for a constant 100 W m^{-2} Q_F directly emitted to the atmosphere over 30 minutes, warming would range from 0.10-0.75 K for UBL heights of 1000 m and 200 m, respectively. This agrees with modelling work that estimates an increase of up to 1.5 K in screen-level air temperature from Q_F during winter nights (Bohnenstengel et al. 2014).

In an ARM context, an increase in daytime air temperature alone would *decrease* Q_H by reducing the vertical gradient between T_0 and T_A . We would expect some corresponding increase in T_0 from Q_F to counteract this, but the location, timing, and magnitude of the surface warming is less well understood. Bohnenstengel et al. (2014) show that approximately 1/3 of Q_F goes into surface heating (and thus outgoing longwave radiation), but that there is a delay of several hours due to the thermal mass of the urban fabric and diffusion of indoor heating sources outwards to exterior building surfaces. Where this warming occurs also has implications for EO-observed LST . If building warming is preferentially directed towards external vertical walls rather than roofs, this may not be captured by downward facing EO sensors with a view-bias towards horizontal rooftops.

To assess whether there are thermal differences in an urban setting attributable to Q_F , observations from the flux tower at KCL in central London data are sorted into working (M-F) and non-working days (S-S and public holidays). Friday evenings (after 19:00 h) are defined as ‘non-working’ and Sunday evenings (after 19:00 h) as ‘working’ (Björkegren and Grimmond 2016). Three winter seasons (DJF 2013-14, 2014-15, 2015-16) are used for analysis because Q_F inputs are expected to be highest relative to Q^* and more easily detected than during other seasons. The 30-minute analysis data are also controlled for $K\downarrow$ (so that hourly median working and non-working day’s $K\downarrow$ values are all within $\pm 5 \text{ W m}^{-2}$) to minimize differences in surface solar energy input.

This analysis shows small but detectable differences in mean hourly air temperature and surface temperature between working and non-working days (Figure 9). Working weekdays tend to have slightly warmer T_R (up to 0.7 K) and air temperatures (up to 0.5 K) compared to weekends and holidays. Working days are generally warmer during daytime with largest differences at midday (1100-1200 UTC). Overnight, weekends and holidays are warmer than working days.

This translates to T_R-T_A differences between working and non-working days as well, with highest differences up to 0.4 K (up to 66%). This vertical gradient equates to Q_H differences of around 20 W m^{-2} during daytime, assuming an r_H value of 25 s m^{-1} representative of winter daytime conditions (Figure 7c). This is comparable to observed eddy covariance Q_H differences of $4.2 - 20.6 \text{ W m}^{-2}$ (0900-1800 UTC).

The diurnal cycles of observed temperature differences are compared to the diurnal cycle of Q_F as modelled by the new version of the Greater Q_F model (Iamarino et al. 2012): GQF (Gabey et al. 2018) within UMEP (Lindberg et al. 2018). The shape of the model diurnal Q_F cycle is based on energy consumption statistics and varies by season, day of week and combination of building sources within an area (Gabey et al. 2018); i.e. KCL tower measurement source areas. Energy consumption statistics demonstrate that Q_F is dominated by building sources and indoor space heating from natural gas combustion. To directly compare the shape of the diurnal course between observed temperature differences and modelled Q_F , both are plotted on the same figure with different y-axes (Figure 9).

From this comparison, we see that modelled Q_F differences follow a diurnal pattern with higher working day (non-working day) values during day (night). Modelled energy consumption differences peak at 09:00 UTC, while peak observed T_A differences occur at 11:00 UTC and T_R differences are at 12:00 UTC. This suggests a lag of 2-3 hours between energy consumption (Q_F emissions) and when external air and surface warming occurs.

There are several implications resulting from this lag. The first is that Q_F emissions are embedded in observed LST and T_A , and thus also Q_H when using ARM; though instantaneous LST (as observed from satellite-platforms) and T_A will not necessarily reflect the actual timing of Q_F emissions. The magnitude of the Q_F contribution to Q_H will depend on the city location and time of day and year and may often only be a minor energy source, especially relative to uncertainties in other aspects with determining Q_H with ARM (Section 3.3-3.4). In principle, this suggests using a residual approach to determine Q_F based on remote sensing is possible (e.g. Chrysoulakis et al. 2015), though current uncertainties in determining Q_H are on the same order of magnitude as the Q_F signal (Section 3.3-3.4).

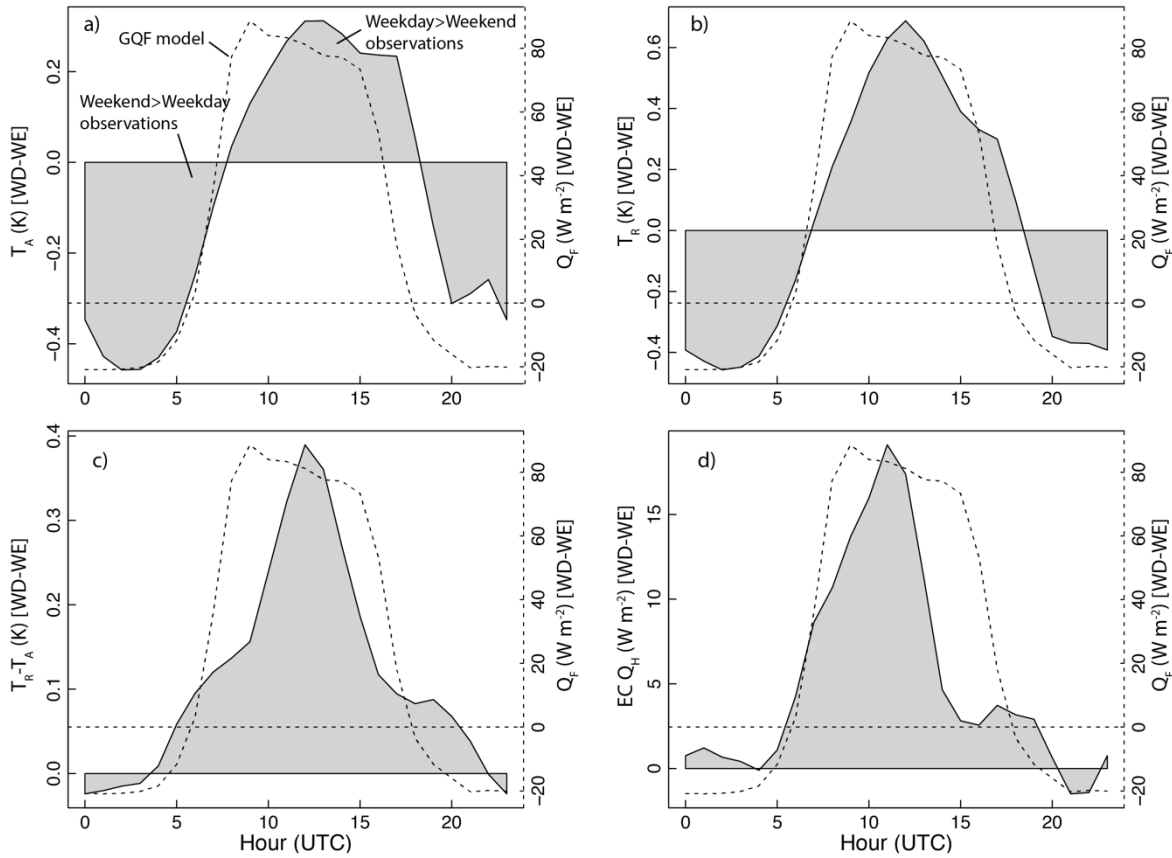


Figure 9. Working (weekday) and non-working (weekend) average differences for a) T_A , b) T_R , c) $T_R - T_A$, and d) eddy covariance Q_H . All data are from the KCL flux tower for 2013–2015 DJF seasons. Results from the energy inventory-based GQF (Iamarino et al. 2012, Gabey et al. 2018, Lindberg et al. 2018) model are shown for reference using second y-axis (dashed line). Note the temperature y-axis ranges for (a)–(c) differ.

3.5 Q_H using ARM

Domain Q_H is calculated with an aerodynamic resistance method (ARM) using observed LST , T_A , and calculated r_H (Section 2.5). A single LST scene (2 Oct 2015, 11:00 UTC) is used as a case study to exemplify results and allow a more detailed spatial view (Figure 10). This period is selected because of high image coverage (97% cloud free) during the satellite overpass and availability of observations from the measurement network for comparison. The day was a working weekday (Friday) with clear skies and mild temperatures (observed 15.7 °C at KCL tower at 11:00 UTC). There was a small amount of precipitation (0.04 mm) recorded the previous day at 15:00 h, but the surface is assumed to have dried by the time of the overpass because this occurred more than 12 hours earlier (Kotthaus and Grimmond 2014). Winds were calm (2.6 m s⁻¹) and from the NE (78°), typical of high-pressure anti-cyclonic synoptic conditions. Sunrise was at 6:02 UTC and solar elevation at the time of the overpass was approximately 30° above the horizon. The previous night was generally clear and calm, allowing for enhanced radiative cooling of the surface overnight.

At the 11:00 UTC overpass, EO-derived LST ranged from 14–28 °C, with cooler temperatures measured generally in vegetated park areas, water bodies, and city centre areas with tallest buildings. T_A varies within a much smaller range (15.6–16.2 °C) compared to LST with cooler values in the city centre associated with higher building heights and thus higher reference height.

Spatial patterns of LST (and input meteorological values) are also manifested in r_H and Q_H . Excluding parks and water bodies, all Q_H methods (R1–R5) show similar spatial pattern of lower values in the city centre and highest values in more vegetated, less densely built areas. This spatial pattern is somewhat counterintuitive as it was expected that highest Q_H would be found in areas with highest built densities with associated higher Bowen ratios and higher Q_F releases compared to less densely built and populated areas. This primarily results from observed LST patterns in central London (Figures 3–6).

Although spatial patterns are similar, there are notably different distributions of pixel-scale Q_H values between the methods. R5 tends to predict highest values compared to the other versions for individual pixels away from the city centre. These values (30% >500 W m⁻² for all 25 scenes) are associated with higher vegetation land cover fractions that result in lower α , lower kB^{-1} , and lower r_H . Whereas, Q_H values determined using R4 appear low for an urban area (25% from 50–100 W m⁻²). This is not unexpected given differences in form (vegetation) and function (Q_F) between the physical model on which R4 is based and the study area, and in Section 3.6 we take advantage of this difference to constrain Q_F estimates.

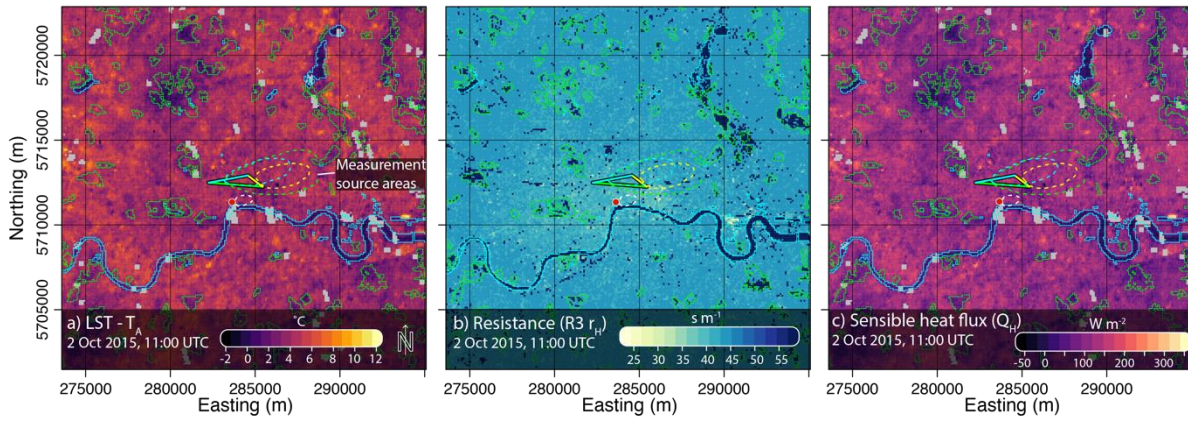


Figure 10. a) $LST-T_A$, b) r_H , and c) Q_H for 11:00 UTC, 2 October 2015 for the R3 method (Table 2). R3 is used as representative of R1-R3 methods (techniques based on central London flux tower observations). Other symbols and outlines are as in Figure 1. Cloud pixels are masked (grey).

To quantify sensitivity of Q_H results to individual input variables for each method, Q_H is modelled with each input variable perturbed individually, while all other variables remain constant (Figure 11). Each variable is perturbed by both a constant $\pm 10\%$ and the uncertainty ranges listed in Table 3. The case study date (2 Oct 2015) is analysed as representative.

Unsurprisingly, all methods are most sensitive to perturbations in LST (± 50 -70%) and to a lesser extent T_A (40-60%) (Figure 11). Q_H is also very sensitive to u^* for methods R2, R4, and R5, as this is used to determine kB^{-1} and gridded wind speed. The R3 method, which uses wind speed as a primary input, is also moderately sensitive to z_0 and z_d . The R5 method is very sensitive to α and λ_V as this determines kB^{-1} and r_H . Results are relatively insensitive to L and surface variables z and z_d .

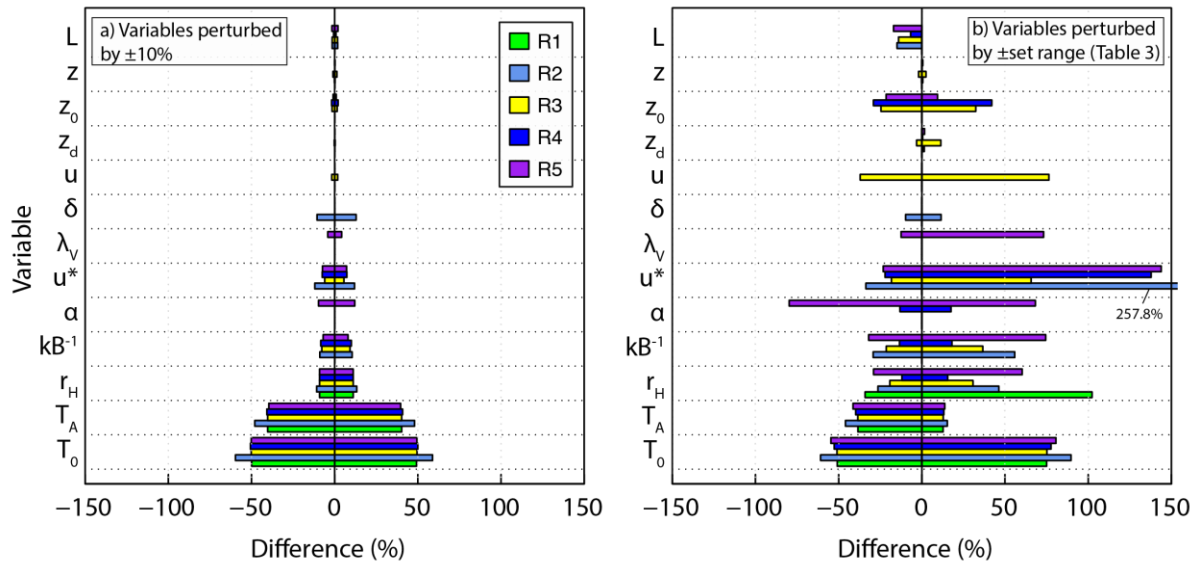


Figure 11. Percentage difference in Q_H for five methods (Tables 2, A2) with individually perturbed input variables and parameters relative to a control run. Each input is perturbed by a) $\pm 10\%$ and by b) prescribed ranges given in Table 3. Also see Table 3 for definition of variables. Note that some methods do not require all variables (Table A.2).

3.6 Comparison to measurements

Each method (R1-R5, Section 2) is compared to observations, to assess the uncertainties and associated assumptions of each. The goal is to understand the urban system based on the entire suite of models, rather than to assign a relative ranking of the models.

Overall, when Q_H is modelled using five methods for all 25 available images, there is an expected annual cycle with highest values generally in the spring (~ 300 -400 $W m^{-2}$, April-May) and lowest values in the autumn and winter (< 150 $W m^{-2}$, October-February) (Figure 3b). Individual R1-R5 results are compared to observations from the three scintillometers and EC station using turbulent flux source area models which vary by observed wind direction and atmospheric conditions (u^* , L , σ_V) at KCL. The source area model of Kormann and Meixner (2001) is used and full details for implementation and weighting along the scintillometer path are described in Crawford et al. (2017). The source area weights for each instrument (100 m resolution) are multiplied by the 100 m Q_H pixels to determine the source area weighted average Q_H to compare with observations.

Overall, R1-R3 (i.e. based on London observations) Q_H compares expectedly reasonably well to observations, though there is scatter about the 1:1 line (Figure 12). For all observations, the lowest mean absolute error (MAE) relative to observations is for R1 (58.1 W m⁻²) (Table 4). The R4 method (Kanda et al. 2007) tends to underestimate observed Q_H by 129.3 W m⁻², on average (Table 4). This too is somewhat expected given differences between the model and real city. We interpret this result as a useful reference or baseline representing Q_H from a non-vegetated city with no active Q_F sources. From this perspective, we can attempt to attribute and constrain contributions of additional energy sources in a real city.

There are likely two primary reasons for the R4-observed difference: 1) vegetation in the real city which acts to lower kB^{-1} and r_H and thus increase Q_H , and 2) Q_F which is embedded in Q_H observations from live cities and therefore also the empirical models based on these observations. Additional physical differences between the model and real world (i.e. building orientation, spacing, and alignment) are less likely to have an appreciable effect. This is based on COSMO model tests with different configurations that demonstrate R4 is applicable over a range of building geometries and alignments (Kanda and Moriizumi, 2009). For vegetation, λ_v in central London is relatively sparse (~0.09) and actual α and kB^{-1} values are lower than expected based purely on this vegetation fraction (Figure 2b).

The primary reason for the discrepancy then may be anthropogenic heat flux (Q_F). The R4 method is based on EC observations from a scale model city with no Q_F sources, whereas the other methods are based on EC observations from real cities which include a portion of Q_F embedded in Q_H measurements. Thus, the R4 method may account for the form but not the functioning of a city and thus underestimates Q_H measurements which include a portion of Q_F in real cities.

To assess if the difference between R4 results and observations could be used to constrain Q_F estimates, total Q_F values were calculated for a subset of overpass times using an independent energy model for spatial areas within the measurement source areas (Gabey et al. 2018). Approximately 80% of total Q_F is expected to be manifest as Q_H , (as noted in Section 3.4; $L\uparrow$, Q_E , ΔQ_S , and waste water also account for the remainder). The GQF model Q_F expressed as Q_H ranges from 111 – 180 W m⁻² and agrees well with the 129.3 W m⁻² MAE between the R4 Q_H model and observations. The same approach also works using the difference between modelled R1 Q_H (constant r_H) and R4 (123.3 W m⁻²). Thus, it appears that the R4 method calculates non-anthropogenic Q_H with no added Q_F component and may have potential as another tool to constrain Q_F , in combination with Q_H observations.

The difference in magnitude of Q_H calculated using winter-observed r_H and summer-observed r_H may also be useful to provide a constraint on Q_F . This is tested with a simple calculation assuming constant ($T_R - T_A$) of 4 °C and typical mid-day winter and summer values of r_H (20 and 50 s m⁻¹, respectively: Figure 7c). This leads to a difference in mid-day Q_H of 144 W m⁻², similar in magnitude to modelled GQF Q_F . The result implies a more efficient heat transfer in winter, but it is unclear if this is from increased Q_F magnitude (but without a corresponding observed change in $T_R - T_A$) or from seasonal differences in turbulence regimes and surface conditions.

Though there is scatter in the comparisons (coefficient of determination R^2 range from 0.42 [R5] to 0.59 [R4]), 80% of all values fall within the 80% uncertainty range (Figure 12) determined from the Monte Carlo sampling technique (Section 2). This implies modelling results are within realistic range of observations, given limitations of the accuracy and resolution of input variables.

Table 4. Observed and source area-averaged model (R1-R5) comparison mean absolute error (MAE) for Q_H . MAE values (W m⁻²) are calculated relative to observations for each sensor and all sensors combined. N = 25 images/time periods.

	P1	P2	P3	EC	All
R1	35.1	56.2	34.2	75.6	58.1
R2	81.6	22.8	45.5	82.9	66.8
R3	47.4	53.2	68.6	73.7	64.5
R4	166.9	97.9	112.8	130.6	129.3
R5	52.8	75.6	62.5	83.6	73.0
R4-5 avg.	33.9	77.9	54.8	64.5	59.3

Based on Monte Carlo analysis of input variables (Table 5), R5 has a broad distribution of values (i.e. more uncertain prediction) because the method relies on several input variables with relatively high degrees of associated uncertainty, particularly u^* , α , and vegetation land cover fraction (Table 3, Section 3.5). R3 has relatively high overall uncertainty due to uncertainties in calculating spatial wind speed variations, which also depend on u^* and z_0 . Probability distributions of R1 and R4 are relatively narrow (i.e. more precise prediction, though not necessarily more accurate) due to reliance on fewer input variables.

Overall, relative uncertainty tends to increase with vegetation land cover fraction (λ_v), particularly for R5 (Figure 13). This is due to the dependence of this method on λ_v to determine α , kB^{-1} , and r_H . Correlation with land cover is less evident with other methods, though the overall uncertainty with R3 is consistently high and R2 and R4 are relatively low. Based on this analysis, we conclude the Kanda et al. (2007) method (R4) performs well at Q_H predictions based on physical form of the city and using an aerodynamic approach. It is of a generalized form for use in a range of cities and is relatively insensitive to variations in meteorological and morphological inputs. However, it is important to note that it is calibrated to a scale model city without Q_F sources (nor vegetation), so predictions are likely of Q_H without additional Q_F inputs found in real cities. Thus, it tends to underestimate observed Q_H in cities which also include a portion of imbedded Q_F . From this perspective, the method also has potential to serve as a baseline reference to assess additional sources of urban energy exchange.

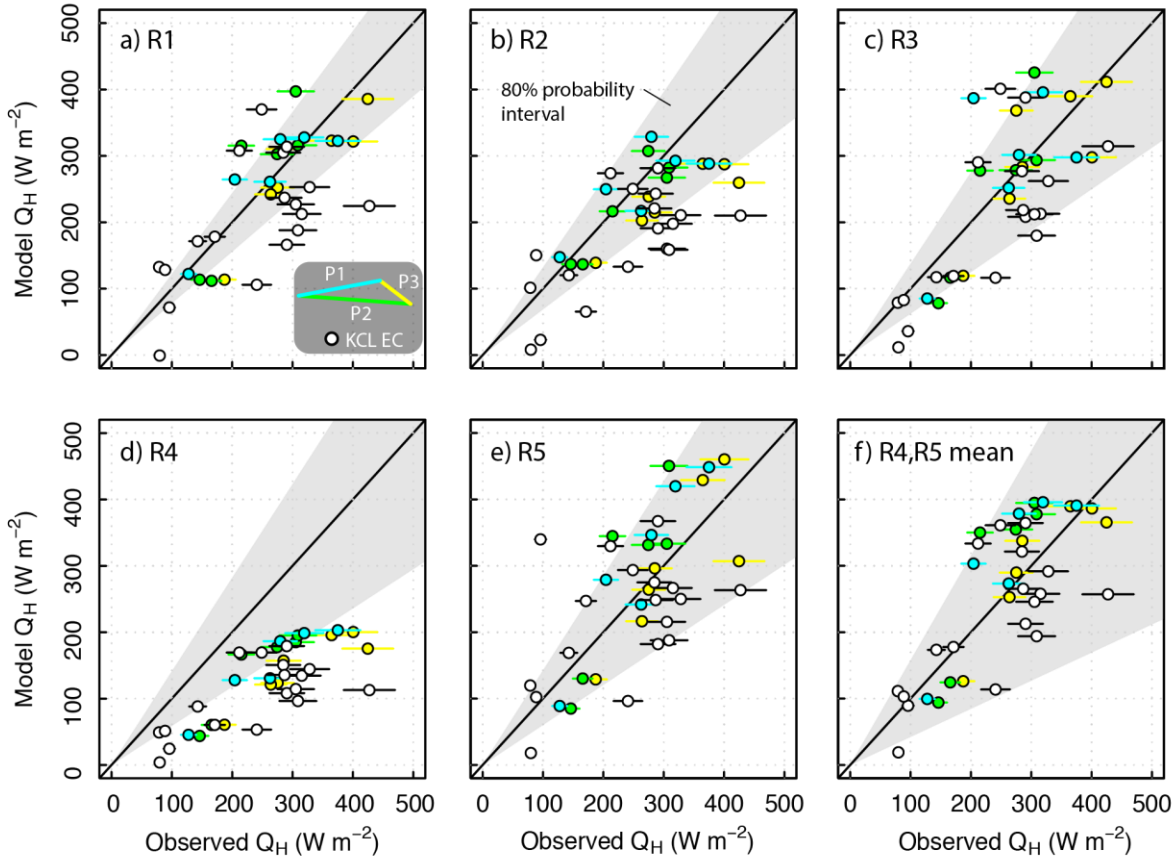


Figure 12. Source area-averaged model Q_H and observations from the scintillometer network (coloured points) and EC tower (white points) with 80% model probability intervals generated for each method (Table 3) from Monte Carlo analysis (grey shaded area). Horizontal error bars are measurement uncertainties (Section 2.2). Comparison statistics are given in Table 4.

Table 5. Absolute and relative Q_H uncertainties for each method (R1-R5, Table 2) for the entire model domain based on Monte Carlo analysis. These values are the mean range of 80% of values for each pixel for each scene based on 20 model runs with varied input parameters.

	R1	R2	R3	R4	R5
Absolute ($W m^{-2}$)	52.8	56.7	78.6	28.2	27.7
Relative (%)	26	46	68	48	51

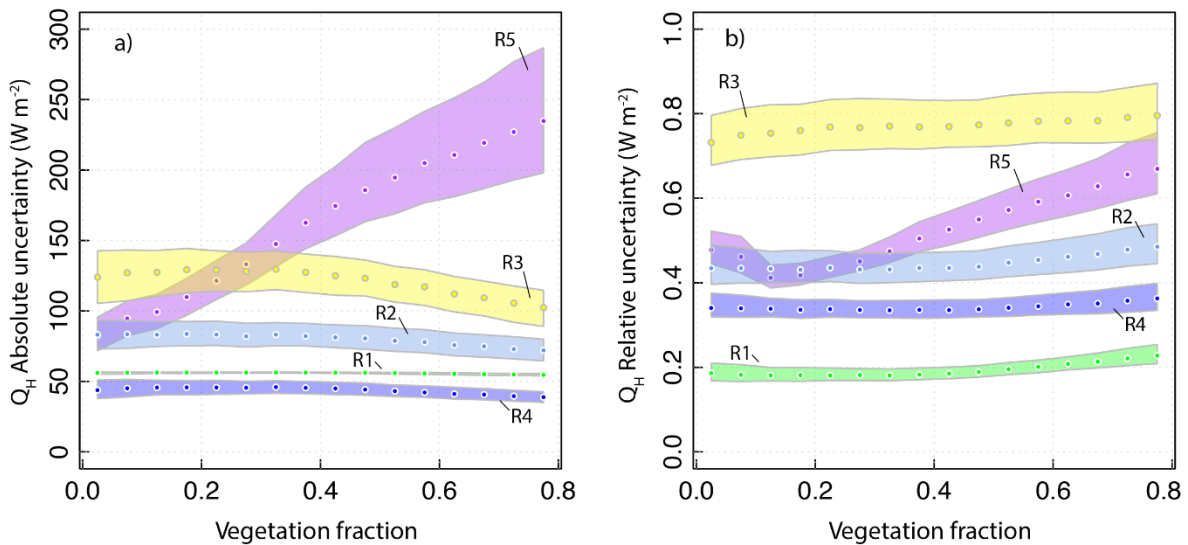


Figure 13. Absolute and relative uncertainty (probability) intervals for ARM-modelled Q_H . The probability interval encloses 80% of Q_H values generated for each pixel based on Monte Carlo analysis for all 25 images. Relative probability interval is defined as the absolute 80% interval range divided by the median for each pixel. Pixels are sorted by vegetation fraction (0.05 bin width) and the interquartile range (shaded area) and median (points) of probability intervals are shown for each resistance method (R1-R5).

4 Conclusions

In this work, we analyse an EO-derived *LST* dataset spanning six years to assess the challenges of using an aerodynamic resistance approach to generate high spatial resolution (100 m) estimates of urban Q_H . A unique feature of this study is the presence of a Q_H measurement network of scintillometers and eddy covariance with which to compare modelled Q_H .

LST spatial patterns are linked with the distribution of vegetation and buildings at the surface. Areas with tall buildings are cooler than average (up to 10%) in *LST* images, but it remains to be seen if this is due to increased shading and reduced sky-view factors or from uncertainties with surface bulk surface emissivity values or satellite view angle bias and thermal anisotropy.

Analysis of T_R and T_A also demonstrates an anthropogenic influence with implications for ARM Q_H . Working weekday T_R and T_A are warmer than weekends and holidays during daytime and there is a lag of 2-3 hours between Q_F emissions (based on energy consumption inventory models) and observed external surface and air warming. This also highlights a shortcoming of using EO-*LST* data: it provides a high spatial resolution snapshot of conditions at a single instant but only provides low temporal resolution.

To determine Q_H from *LST*, five thermal resistance methods are compared. Three (R1-R3) are based on empirical relations observed at a central London EC tower: i) observed diurnal cycle of r_H , ii) a linear relation between measured wind speed and z_H , and iii) a linear relation between solar elevation and z_H .

Analysis to derive these relations demonstrate that r_H , kB^{-1} , and z_H vary on diurnal and seasonal timescales. Diurnally, r_H and kB^{-1} are greatest, and z_H is least, during mid-day periods. This is reasoned to be because momentum transfer is enhanced relative to heat transfer in urban areas due to pressure drag from bluff bodies. Although Q_H is also greatest during mid-day periods, the momentum transfer is comparatively greater. In general, observations of z_H in urban areas are rare and its variability is poorly understood. Here we show z_H varies diurnally according to wind speed, turbulence, solar angle and atmospheric stability.

Observations and models of Q_H using these methods are in general agreement, though there is scatter in the linear comparisons. Model results are found to be sensitive to uncertainties in T_0 and input meteorological variables needed to estimate r_H (u , u^* , T_A). However, based on Monte Carlo sampling of these variables within prescribed ranges, 80% of comparisons are within 80% confidence intervals.

Two previously published empirical relations are also tested, derived from observations based on: i) a physical scale urban model (R4) (Kanda et al. 2007) and ii) from several real cities (R5) (Kawai et al. 2009). For the R4 method, differences between observations are most likely due to the influence of Q_F on observations. Since the model coefficients are calibrated to a scale model with no Q_F sources, results using this method may underestimate Q_H observations in a real city, which include a portion of Q_F . Thus, this method may have potential to act as a baseline reference and constrain estimates of energy partitioning between Q_H and Q_F .

For the R5 method, pixels with greater vegetation land cover tend to produce unrealistically high Q_H values. This is largely due to uncertainties in determining kB^{-1} parameters across the full spectrum of urban forms and neighbourhood types.

In general, R4 (Kanda et al. 2007) is suitable to calculate r_H because of its generalized urban form and high precision due to reliance on relatively few input variables. This work also highlights the need for further measurements in contrasting urban environments: particularly in areas with tall, dense buildings and neighbourhoods with high vegetation density. Ideally a range of observations that include a range of urban form (e.g. denser/lighter building materials; smaller/larger buildings) and function (e.g. more/less Q_F) with changing wind flow regimes (i.e. roughness element packing) would allow a systematic assessment of the controls on r_H prior to adding the vegetation effects.

Overall, an aerodynamic resistance approach remains a useful, conceptually straight-forward way to estimate bulk Q_H in urban areas. However, the approach is sensitive to several input variables (e.g. u^*), so practical challenges remain in resolving spatial variations in urban surface and meteorological conditions in urban areas. Thus, in future studies a more probabilistic approach to modelling urban energy fluxes may be advantageous in the face of these uncertainties.

5 Acknowledgments

This work is funded by European Union Horizon 2020 UrbanFluxes, the Newton Fund/Met Office CSSP-China, NERC ClearfLo, NERC TRUC, and NERC AirPro. We are very grateful to BT, Islington Council, Barbican, and King's College London for site access. Kjell zum Berge, Ting Sun, William Morrison, Natalie Theeuwes, and Simone Kotthaus (University of Reading) and Makoto Nakayoshi (Tokyo University of Science) made valuable contributions to fieldwork and discussions.

6 References

- Arnfield, A. J. "An approach to the estimation of the surface radiative properties and radiation budgets of cities." *Physical Geography* 3.2 (1982): 97-122.
- Barlow J, Best M, Bohnenstengel SI, Clark P, Grimmond S, Lean H, Christen A, Emeis, S, Haeffelin M, Harman IN, Lemonsu A, Martilli A, Pardyjak E, Rotach MW, Ballard S, Boutle I, Brown A, Cai X, Carpentieri M, Coccal O, Crawford B, Di Sabatino S, Dou J, Drew D, Edwards JM, Fallmann J, Fortuniak K, Gornall J, Gronemeier T, Halios C, Hertwig D, Hirano K, Holtslag AAM, Luo Z, Mills G, Nakayoshi M, Pain K, Schlünzen KH, Smith S, Soulhac L, Steeneveld G-J, Sun T, Theeuwes N, Thomson D, Voogt JA, Ward H, Xie Z-T, Zhong J 2017: The integration of urban atmospheric processes across scales. *BAMS*, **98**, ES261–ES264 [doi:10.1175/BAMS-D-17-0106.1](https://doi.org/10.1175/BAMS-D-17-0106.1)

- Best, M. J., and C. S. B. Grimmond. "Key conclusions of the first international urban land surface model comparison project." *Bulletin of the American Meteorological Society* 96.5 (2015): 805-819.
- Brutsaert, W. H. "Evaporation in the Atmosphere." D. Reidel (1982).
- Chen, Yingying, et al. "Improving the Noah land surface model in arid regions with an appropriate parameterization of the thermal roughness length." *Journal of Hydrometeorology* 11.4 (2010): 995-1006.
- Christen, Andreas, and Roland Vogt. "Energy and radiation balance of a central European city." *International journal of climatology* 24.11 (2004): 1395-1421.
- Chrysoulakis, N., Heldens, W., Gastellu-Etchegorry, J.P., Grimmond, S., Feigenwinter, C., Lindberg, F., Del Frate, F., Klostermann, J., Mitraka, Z., Esch, T. and Al Bitar, A., 2015. Urban Energy Budget Estimation from Sentinels: The URBANFLUXES Project. *Mapping Urban Areas from Space*.
- Crawford B, CSB Grimmond, HC Ward, W Morrison, S. Kotthaus 2017: Spatial and temporal patterns of surface-atmosphere energy exchange in a dense urban environment using scintillometry *QJRMS*, 143, 703, B, 817–833 [10.1002/qj.2967](https://doi.org/10.1002/qj.2967)
- Crawford, B., and A. Christen. "Spatial source attribution of measured urban eddy covariance CO₂ fluxes." *Theoretical and Applied Climatology* 119.3-4 (2015): 733-755.
- Crawford, B, C. S. B. Grimmond, and A Christen. "Five years of carbon dioxide fluxes measurements in a highly vegetated suburban area." *Atmospheric Environment* 45.4 (2011): 896-905.
- Del Frate, Fabio, W. Heldens, N. Chrysoulakis, F. Lindberg, Z. Mitraka, C.S.B. Grimmond, A. Gabey, F. Olofson, D. Poursanidis, C. Feigenwinter, A. Albitar, D. Latini. Urban surface morphology land cover/use and characteristics. UrbanFluxes Report D3.1 (2016). DLR 2012, http://www.dlr.de/eoc/Portaldata/60/Resources/dokumente/5_tech_mod/atcor3_manual_2012.pdf Accessed 24 July 2016
- Gabey A, S Grimmond, I Capel-Timms (2018) Anthropogenic Heat Flux: At what spatial resolution is a simple model reasonable? *Theoretical and Applied Climatology* doi: 10.1007/s00704-018-2367-y
- Gabey A., S. Grimmond. 'Availability, evaluation and synthesis of metadata describing Citizen Weather Stations', In preparation.
- Gerace, A., & Montanaro, M. (2017). Derivation and validation of the stray light correction algorithm for the thermal infrared sensor onboard Landsat 8. *Remote Sensing of Environment*, 191, 246-257.
- GLA Datastore (2017), accessed 19 May, 2017. <https://data.london.gov.uk/dataset/interim-2015-based-population-projections/resource/4fcb8bfa-f860-48cc-af96-44a0931e4f27#>
- Grimmond, CSB, and TR Oke. "Aerodynamic properties of urban areas derived from analysis of surface form." *Journal of applied meteorology* 38.9 (1999): 1262-1292.
- Grimmond, C. S. B., M. Blackett, M. J. Best, J-J. Baik, S. E. Belcher, J. Beringer, S. I. Bohnenstengel et al. "Initial results from Phase 2 of the international urban energy balance model comparison." *International Journal of Climatology* 31, no. 2 (2011): 244-272.
- Heidbach, Katja, Hans Peter Schmid, and Matthias Mauder. "Experimental evaluation of flux footprint models." *Agricultural and Forest Meteorology* 246 (2017): 142-153.
- Högström, U. L. F. "Non-dimensional wind and temperature profiles in the atmospheric surface layer: A re-evaluation." *Topics in Micrometeorology. A Festschrift for Arch Dyer*. Springer Netherlands, 1988. 55-78.
- Iamarino, M., S. Beevers and C. S. B. Grimmond (2012). "High-resolution (space, time) anthropogenic heat emissions: London 1970–2025." *International Journal of Climatology* 32(11): 1754-1767.
- Kato, S., & Yamaguchi, Y. (2005). Analysis of urban heat-island effect using ASTER and ETM+ Data: Separation of anthropogenic heat discharge and natural heat radiation from sensible heat flux. *Remote Sensing of Environment*, 99(1), 44-54.
- Kanda, M., et al. "Roughness lengths for momentum and heat derived from outdoor urban scale models." *Journal of Applied Meteorology and Climatology* 46.7 (2007): 1067-1079.
- Kanda, Manabu, et al. "A new aerodynamic parametrization for real urban surfaces." *Boundary-layer meteorology* 148.2 (2013): 357-377.
- Kanda, M., Kawai, T., Kanega, M., Moriwaki, R., Narita, K., & Hagishima, A. (2005). A simple energy balance model for regular building arrays. *Boundary-Layer Meteorology*, 116(3), 423-443.
- Kanda, M., & Moriizumi, T. (2009). Momentum and heat transfer over urban-like surfaces. *Boundary-layer meteorology*, 131(3), 385-401.
- Kastner-Klein, Petra, and Mathias W. Rotach. "Mean flow and turbulence characteristics in an urban roughness sublayer." *Boundary-Layer Meteorology* 111.1 (2004): 55-84.
- Kawai, T., M. K. Ridwan, and M Kanda. "Evaluation of the simple urban energy balance model using selected data from 1-yr flux observations at two cities." *Journal of Applied Meteorology and Climatology* 48.4 (2009): 693-715.
- Kent, C. W., Grimmond, S., Barlow, J., Gatey, D., Kotthaus, S., Lindberg, F., & Halios, C. H. (2017). Evaluation of Urban Local-Scale Aerodynamic Parameters: Implications for the Vertical Profile of Wind Speed and for Source Areas. *Boundary-Layer Meteorology*, 164, 183–213 doi: [10.1007/s10546-017-0248-z](https://doi.org/10.1007/s10546-017-0248-z).
- Kormann, Robert, and Franz X. Meixner. "An analytical footprint model for non-neutral stratification." *Boundary-Layer Meteorology* 99.2 (2001): 207-224.
- Kotthaus, S., Smith, T. E., Wooster, M. J., & Grimmond, C. S. B. (2014). Derivation of an urban materials spectral library through emittance and reflectance spectroscopy. *ISPRS Journal Of Photogrammetry And Remote Sensing*, 94, 194-212.
- Kotthaus, Simone, and C. S. B. Grimmond. "Energy exchange in a dense urban environment–Part II: Impact of spatial heterogeneity of the surface." *Urban Climate* 10 (2014): 281-307.
- Lagouarde, J-P., et al. "Modelling daytime thermal infrared directional anisotropy over Toulouse city centre." *Remote Sensing of Environment* 114.1 (2010): 87-105.
- Lindberg, F., F. Olofson, T. Sun, C.S.B. Grimmond, C. Kent, W. Morrison. "Assessment and evaluation of ΔQs using different methods." UrbanFluxes Report D5.2 (2016)
- Lindberg, Fredrik, and C.S.B. Grimmond. "Nature of vegetation and building morphology characteristics across a city: influence on shadow patterns and mean radiant temperatures in London." *Urban Ecosystems* 14.4 (2011): 617-634.
- Lindberg F, CSB Grimmond, A Gabey, B Huang, CW Kent, T Sun, NE Theeuwes, L Järvi, H Ward, I Capel-Timms, YY Chang, P Jonsson, N Krave, DW Liu, D Meyer, KFG Olofson, JG Tan, D Wästberg, L Xue, Z Zhang 2018: Urban multiscale environmental predictor (UMEP) - An integrated tool for city-based climate services *Environmental Modelling and Software* 99, 70–87 [10.1016/j.envsoft.2017.09.020](https://doi.org/10.1016/j.envsoft.2017.09.020)
- London Grid for Learning, 2016. <https://weather.lgfl.org.uk/> . Accessed 24 July 2016

- Mahrt, L. "The bulk aerodynamic formulation over heterogeneous surfaces." Boundary-Layer Meteorology 25th Anniversary Volume, 1970–1995. Springer Netherlands, 1996. 87-119.
- Marconcini, Mattia, Wieke Heldens, Fabio Del Frate, Daniele Latini, Zina Mitranka, and Fredrik Lindberg. "EO-based products in support of urban heat fluxes estimation." In *Urban Remote Sensing Event (JURSE), 2017 Joint*, pp. 1-4. IEEE, 2017.
- Met Office, 2016 <http://www.metoffice.gov.uk/datapoint> .Accessed 24 July 2016
- Mitraka, Zina, Nektarios Chrysoulakis, Yiannis Kamarianakis, Panagiotis Partsinevelos, and Androniki Tsouchlaraki. "Improving the estimation of urban surface emissivity based on sub-pixel classification of high resolution satellite imagery." *Remote Sensing of Environment* 117 (2012): 125-134.
- Moriwaki, Ryo, and Manabu Kanda. "Scalar roughness parameters for a suburban area." *Journal of the Meteorological Society of Japan. Ser. II* 84.6 (2006): 1063-1071.
- Morrison W. S Kotthaus; S Grimmond; Atsushi Inagaki; Tiangang Yin; Jean-Philippe Gastellu-Etchegorry; Manabu Kanda; Christopher Merchant Longwave radiation fluxes observed with ground-based thermography to model urban thermal anisotropy, *Remote Sensing of Environment* (in review)
- Netatmo, 2016. www.netatmo.com . Accessed 24 July 2016
- Owen, P. R., and W. R. Thomson. "Heat transfer across rough surfaces." *Journal of Fluid Mechanics* 15.03 (1963): 321-334.
- Ordnance Survey MasterMap, <https://www.ordnancesurvey.co.uk/business-and-government/products/mastermap-products.html>, Accessed 11 August 2016
- Roth, Matthias. "Review of atmospheric turbulence over cities." *Quarterly Journal of the Royal Meteorological Society* 126.564 (2000): 941-990.
- Schmid, H. P. "Source areas for scalars and scalar fluxes." *Boundary-Layer Meteorology* 67.3 (1994): 293-318.
- Small, Christopher. "Multitemporal analysis of urban reflectance." *Remote Sensing of Environment* 81.2 (2002): 427-442.
- SPOT 2016, <http://www.intelligence-airbusds.com/> Accessed 25 July 2016
- Stull, Roland B. An introduction to boundary layer meteorology. Vol. 13. Springer Science & Business Media, 2012.
- Sugawara, Hirofumi. "Heat exchange between urban structures and the atmospheric boundary layer." *Doctoral Dissertation Tohoku Univ.* (2001).
- Sun, Jielun. "Diurnal variations of thermal roughness height over a grassland." *Boundary-Layer Meteorology* 92.3 (1999): 407-427.
- Theeuwes, N. E., Steeneveld, G. J., Ronda, R. J., Rotach, M. W., & Holtslag, A. A. (2015). Cool city mornings by urban heat. *Environmental Research Letters*, 10(11), 114022.
- USGS 2016 <http://landsat.usgs.gov/landsat8.php> Accessed 24 July 2016
- van der Loo, M., 2010. Extreme values, an R package for outlier detection in univariate data. *R package version*, 2.
- Van Ulden, A. P., and A. A. M. Holtslag. "Estimation of atmospheric boundary layer parameters for diffusion applications." *Journal of Climate and Applied Meteorology* 24.11 (1985): 1196-1207.
- Verma, S. B. "Aerodynamic resistances to transfers of heat, mass and momentum." *Estimation of areal evapotranspiration* 177 (1989): 13-20.
- Voogt, James A., and C. S. B. Grimmond. "Modeling surface sensible heat flux using surface radiative temperatures in a simple urban area." *Journal of Applied Meteorology* 39.10 (2000): 1679-1699.
- Voogt, James A., and Tim R. Oke. "Thermal remote sensing of urban climates." *Remote sensing of environment* 86.3 (2003): 370-384.
- Ward, H. C., J. G. Evans, and C. S. B. Grimmond. "Multi-season eddy covariance observations of energy, water and carbon fluxes over a suburban area in Swindon, UK." *Atmospheric Chemistry and Physics* 13.9 (2013): 4645-4666.
- Ward, Helen C. "Scintillometry in urban and complex environments: a review." *Measurement Science and Technology* 28.6 (2017): 064005.
- Weather Underground, 2016. www.wunderground.com . Accessed 24 July 2016
- Weng, Q., Hu, X., Quattrochi, D. A., & Liu, H. (2014). Assessing intra-urban surface energy fluxes using remotely sensed ASTER imagery and routine meteorological data: A case study in Indianapolis, USA. *IEEE Journal of Selected Topics in Applied Earth Observations and Remote Sensing*, 7(10), 4046-4057.
- Yang, K., Koike, T., Ishikawa, H., Kim, J., Li, X., Liu, H., Liu, S., Ma, Y. and Wang, J., 2008. Turbulent flux transfer over bare-soil surfaces: characteristics and parameterization. *Journal of Applied Meteorology and Climatology*, 47(1), pp.276-290.